

Modelling electrical transport in nano-particle composites using 3D network analysis

by

Kaan Owen Williams

B.A.Sc., The University of British Columbia, 2009

A THESIS SUBMITTED IN PARTIAL FULFILLMENT OF
THE REQUIREMENTS FOR THE DEGREE OF

MASTER OF APPLIED SCIENCE

in

The Faculty of Graduate and Postdoctoral Studies

(Electrical & Computer Engineering)

THE UNIVERSITY OF BRITISH COLUMBIA

(Vancouver)

February 2014

© Kaan Owen Williams, 2014

Abstract

Conductive composites consist of a conductive filler dispersed within an insulating matrix. These composite materials have been known for many years and are regularly produced experimentally and commercially for a variety of applications. Novel techniques are now being found for creating composites that exhibit conductivity with less conductive filler material than classical physics suggests is sufficient if the particles are uniformly distributed. Several parties have offered physical explanations for the characteristics of their composites by incorporating a blend of classical and quantum physics but few attempts have been made to compare explanations or develop any mechanism to simulate the physics. The model presented in the present work incorporates first principles physics and semi-empirical theory to account for the distribution of particles within a composite and calculate resultant conductivity using three dimensional network analysis. Results from several model iterations are presented and they are compared with published experimental results. The model demonstrates that a random distribution of spherical particles smaller than 200 nm at 3% loading, given realistic wave function decay rates and reasonable tunnelling barrier heights, cannot explain experimentally observed conductivities in these composite materials. The final model, using a Voronoi tessellation approach, duplicates the behaviour trend of the composites being simulated and illustrates some gaps in the present material science knowledge of conductive composites.

Preface

Early work on the model presented herein was performed by Liam Russel in 2010. His initial MATLAB embodiment was limited to the particle placement method described in Section 2.1.1 and was limited to simulations involving relatively few particles within relatively small volumes. Nevertheless his framework established an approach that was substantially continued as the present model was developed. In cases where the algorithms developed by Russel did not need logical adjustment (such as the particle connectivity mapping described in Section 2.2) his code was re-written or adapted to improve memory usage and computation time at larger scales. The only component that remained substantially unchanged is used to graphically display model output. That component proved useful during the work discussed herein although it was not used to generate any of the figures presented.

Figures 1.7 and 1.9 are used with permission from applicable sources. Figure 1.6 was generated by me to show a subset of the information presented in a similar figure published by Kohjiya *et al.* and he is credited in that figure's caption.

A series of material analyses performed by Aaron Linklater cited in Figure 1.8 and elsewhere are unpublished and were shared through an internal UBC report.

Table of contents

Abstract	ii
Preface	iii
Table of contents	iv
List of tables	vi
List of figures	vii
List of symbols	xii
List of abbreviations	xiv
Acknowledgements	xv
Dedication	xvi
1 Background	1
1.1 Percolation	1
1.2 Tunnelling conduction	3
1.2.1 Sphere to sphere tunnelling	3
1.2.2 Hard/soft shell approach	10
1.3 Particle agglomeration and filament formation	12
1.4 Carbon black as a conductive filler	12
1.5 Summary	18
2 Experimental methods	19
2.1 Particle placement	21
2.1.1 Method 1: random placement of uniform particles	21
2.1.2 Method 2: clustering	21
2.1.3 Method 3: volume exclusion method	22
2.1.4 Method 4: Voronoi wire frame method	23

Table of contents

2.1.5	Method 5: distributed radii	25
2.1.6	Method 6: intersections allowed	26
2.2	Particle connectivity mapping	28
2.3	Electrodes	29
2.4	Node trimming	29
3	Inter-particle conductivity	32
3.1	Absolute path length	32
3.2	Basic exponential	32
3.3	Conduction due to particle contact	33
3.4	Conductivity summary	34
4	Results	37
4.1	Model size	37
4.2	Random placement of uniform particles	37
4.3	Contact conduction	39
4.4	Clustering and filaments	43
4.5	Voronoi cell network	50
5	Conclusions and future work	56
5.1	Conclusions	56
5.2	MATLAB as a modelling tool	57
5.3	Future work	58
5.3.1	Greater complexity in modelling parameters	58
5.3.2	Post-curing analysis of carbon black	58
5.3.3	Alternate techniques	59
	Bibliography	60
	 Appendix	
A	Simulation parameters	66

List of tables

1.1	Comparison of values for φ and δ	8
-----	---	---

List of figures

1.1	Figure 1.1A is an illustration showing the basic power law relationship described by combining equation (1.1) (solid line) and equation (1.2) (dashed line). In this illustration $\phi_c = 0.16$ and $t = 2.0$ are used and σ is scaled for visual clarity. Figure 1.1B does not differentiate between equation (1.1) and equation (1.2) but shows the effect of scaling t . For the dotted line $t = 1.5$, for solid line $t = 2$, and for the dashed line $t = 2.5$.	2
1.2	Equation 1.3 is represented by $\frac{1}{R_\delta}$ as a function of δ with lines shown for four different values of φ . In this example $A = \pi(10 \text{ nm})^2$.	5
1.3	Comparison of potential barrier height and the constant γ according to equation (1.4). Recall that potential barriers in conductive composites are typically in the range $0.05 \text{ eV} > \varphi > 1 \text{ eV}$ [1]. The boundaries of that range are illustrated with dotted lines for reference.	6
1.4	Comparison of potential barrier height (φ) and the inter-particle gap over which tunnelling must typically occur (δ) using the modelling approach from Wang <i>et al.</i> [2] and Meier <i>et al.</i> [3].	9
1.5	The normalised critical distance, $\frac{\delta_c}{2r}$, is shown with respect to volume loading fraction of solid core spheres. The relationship is described explicitly by equations (1.15) and (1.16) taken from [4].	11
1.6	Typical distance between nearest-neighbour carbon black agglomerates in natural rubber as a function of volume loading fraction. Adapted from [5].	14
1.7	Scanning electron microscope micrograph of Vulcan XC72. Reprinted from [6] with permission from Elsevier.	15

1.8	Conductivity across a range of loadings of two different carbon blacks in four different polymers. Taken from works published or shared by Niu <i>et al.</i> [7], Rwei <i>et al.</i> [8], Linklater [9], Li [10], Huang [11], and Huang <i>et al.</i> [12].	17
1.9	Size distribution of Vulcan XC72. Data represents about 660 particles in about 200 images. Figure created by [13]. Reprinted by permission of The Electrochemical Society.	18
2.1	Processing the present model involves six steps that are described in the text.	20
2.2	A two dimensional arbitrary unit representation of the volume exclusion method described in Section 2.1.3. Exclusion zones are shown as circles with a dashed line (radius = 0.05). Particles are shown as a circle with a solid line (radius = 0.01). In this example, exclusions zones are permitted to overlap, particles are not, and no particles may be in an exclusion zone.	23
2.3	A 2D Voronoi structure with cell edges shown as lines and dots at each seed point.	24
2.4	Stereographic example of a 3D Voronoi structure with cell edges shown as lines and dots at each vertex. Seed points are shown as a star. Hold image about 50 cm away and allow eyes to cross slightly. When three images appear, observe the central one.	25
2.5	In this example set of particles the user set target mean radius and standard deviation were 65.0 nm and 9.75 nm respectively. A log-normal distribution with those parameters is shown as a dashed line for reference. It has a mode radius of about 62.8 nm. The resultant particles from four successive models are combined and histogram data of the resultant radius distribution is shown as the solid line. Histogram bins span about 0.32 nm. Particle radii vary from 31.2 nm to 124.5 nm with a mean and standard deviation of 64.3 nm and 9.55 nm respectively.	27

2.6	In this two dimensional arbitrary unit example conductive particles are shown as \cdot and electrodes are shown as $*$. Connections between sites (particles or electrodes) are shown as a line. Diagram A shows a connected network that has few electrode connection sites. Diagram B shows the same network but with more electrode connection sites. Observe the difference between the two diagrams in particular near x-axis locations 0.2, 0.5, and 0.8.	30
2.7	This two dimensional arbitrary unit example contains the same connected network as Figure 2.6B. Conductive particles are shown as \cdot and electrodes are shown as $*$. Connections between sites (particles or electrodes) are shown as a line. Three particle sites that do not contribute useful electrical nodes have been identified (with circles) as suitable for exclusion from the conductivity calculation.	31
3.1	Geometry between overlapping spheres, $\delta < 0$. When $\delta > 0$, $r_c = 0$, and the spheres do not overlap.	34
3.2	Conductance between particles arranged according to increasing gap size. Particle size varies as illustrated in Figure 2.5 and the effect of this variation can be seen as a small amount of noise in the line. A negative gap indicates particles overlap and the particles are therefore in physical contact.	36
4.1	Conductivity is shown to increase asymptotically to a maximum value as the edges length of a cube being simulated increases. Individual results are shown as a circle. The long-dash line indicates mean value and the dotted lines are one standard deviation above and below the mean. The solid line shows the exponential increase in computation time as the edge size increases.	38
4.2	Particles that are deemed “connected” will conduct charge according to equation (3.2). The amount of conduction that occurs depends on the gap between particles. The right axis (and thin line) show histogram counts for gaps of a particular length from a typical execution of the model. Histogram bins span about 5.5 nm. For reference, the left axis (and thick dashed line) show the results of the tunnelling equation (3.2) for a gap of that size.	40

- 4.3 Five unique models were created with the same initial parameters (described in the text). Once each model was created, the radius of interaction was varied to create maps of connected particles. If a model exhibited end-to-end connectivity of its particles at a particular radius of interaction, a conductivity value for that combination is shown. Data to the left of the vertical dashed line is intermittent and data to the right of the vertical dashed line begins to converge. 41
- 4.4 Particles with a negative inter-particle distance are said to be in contact and conduct according to equation (3.11). Particles not in physical contact that are deemed “connected” will conduct charge according to equation (3.2). The right axis (and thin line) show histogram counts for gaps of a particular length from a typical execution of the model. Histogram bins span about 5.8 nm. The left axis (and thick dashed line) show the results of the contact equation (3.11) and tunnelling equation (3.2) for a gap of that size. 42
- 4.5 Five unique models were created with nearly all the same initial parameters to generate each set of results (each set is shown with a different symbol). The only difference between each set of model parameters is the numerical value for γ (indirectly defined by setting the barrier height to three different values). For \diamond , $\varphi = 0.1$ meV. For \circ , $\varphi = 1$ μ eV. For $*$, $\varphi = 10$ neV. Once each model was created, the radius of interaction was varied to create maps of connected particles. If a model exhibited end-to-end connectivity of its particles at a particular radius of interaction, a conductivity value for that combination is shown. Data to the left of the vertical dashed line is noisy and intermittent and data to the right of the vertical dashed line begins to converge. 44
- 4.6 Three hundred particles are distributed in two dimensional space (arbitrary units). Seventy five of them are placed randomly and the remainder are placed in succession where each must be within 0.5 units of a previously placed particle. Each particle is shown as \cdot and its radius of interaction is shown as \circ ($r_i \approx 0.015$ units). For the purposes of this illustration, consider particles connected if their \circ 's touch. The result is similar to a random distribution. Some connections exist but rarely involving many particles. 46

4.7	Three hundred particles are distributed in two dimensional space (arbitrary units). Seventy five of them are placed randomly and the remainder are placed in succession where each must be within 0.05 units of a previously placed particle. Each particle is shown as \cdot and its radius of interaction is shown as \circ ($r_i \approx 0.015$ units). For the purposes of this illustration, consider particles connected if their \circ 's touch. Several groupings of many particles are apparent but the groupings do not often interconnect.	47
4.8	Conductivity values as a function of radius of interaction when an enforced proximity of 25 nm is implemented. Each data point represents the mean result of five simulations and each line is associated with a different enforcement probability as shown in the legend. Overall volume loading of particles is held constant at $\phi = 0.03$. As described in Section 2, conductivities near 10^{-9} S/m are of unreliable precision due to a near-singularity during matrix inversion. This accounts for the erratic low mean conductivity values.	48
4.9	Conductivity values as a function of radius of interaction when an enforced proximity of 100 nm is implemented. Each data point represents the mean result of five simulations and each line is associated with a different enforcement probability as shown in the legend. Overall volume loading of particles is held constant at $\phi = 0.03$	49
4.10	Histogram data of typical mean edge lengths for a model with a target density of $v_{dens} = 5 \times 10^6$ mm ⁻³ . Each histogram bin spans about 0.95 μ m.	50
4.11	Conductivity as a function of volume loading for a range of filament radius values.	52
4.12	Model results are shown here with published experimental data [8, 9]. (Individual attributions are shown in Figure 1.8.) Model results are those previously shown in Figures 4.3, 4.5, 4.9, and 4.11. For reference, the upper limit of conductivity is also shown.	53
4.13	Voronoi model results are compared to a line fit for the power law behaviour discussed in Section 1.1.	54
4.14	Conductivity as a function of radius of interaction for four different volume loadings. Data to the lower-left of the dashed line is noisy and intermittent in end-to-end connectivity and data to the upper-right of the dashed line is convergent. . . .	55

List of symbols

Symbol	Units	Description
A	m^2	effective cross-sectional area where tunnelling occurs
A_c	m^2	cross-sectional area of particle contact
a	m	distance between sphere-centres
a_0		fitting constant
a_1		fitting constant
a_2		fitting constant
a_3		fitting constant
C_δ	F	capacitance between two sites separated by δ
f		denotes a function defined elsewhere
f_0	s^{-1}	resonant frequency
G	S	conductance
G_t	S	inter-particle tunnelling conductance
G_0	S	base conductance
G_1	S	filler conductance
G_c	S	contact conductance
m_e	kg	electron mass $\approx 9.11 \times 10^{-31}$
n		number of particles
q_e	C	elementary charge $\approx 1.60 \times 10^{-19}$
R_δ	Ω	resistance between two sites separated by δ
R_0	Ω	characteristic resistance
r	m	radius of a spherical conductive particle
r_1	m	radius of sphere one
r_2	m	radius of sphere two
r_c	m	radius of the contact circle made by two overlapping spheres
r_i	m	radius of interaction
t		critical exponent of conductance
V	m^3	volume
v_{dens}	m^{-3}	quantity of Voronoi cells per unit volume
v_{rMax}	m	maximum thickness of filaments in Voronoi cells
δ	m	distance between conductive particles

List of symbols

δ_c	m	critical distance
γ	m^{-1}	wave function decay rate
ϵ		relative permittivity
ϵ_0	$\text{A}^2 \text{S}^4 \text{kg}^{-1} \text{m}^{-3}$	vacuum permittivity $\approx 8.85 \times 10^{-12}$
θ	rad	angle considered in Figure 3.1
ξ	m	characteristic tunnelling length
π		ratio of a circle's circumference to its diameter ≈ 3.14
σ	S m^{-1}	conductivity
σ_c	S m^{-1}	internal conductivity of conductive particles
σ_δ	S m	conductivity of a fixed cross-sectional area
ϕ		volume fraction of conductive particles within an insulator
ϕ_c		critical volume fraction of conductive particles within an insulator
φ	eV	potential barrier height
\hbar	$\text{m}^2 \text{kg s}^{-1}$	reduced Planck constant $\approx 1.05 \times 10^{-34}$
%		parts per hundred

List of abbreviations

Abbreviation	Description
2D	two dimensional
3D	three dimensional
A	amp
C	coulomb
cm	centimetre
cos	cosine
eV	electron-volt
F	farad
GB	gigabyte
GHz	gigahertz
Hz	hertz
kg	kilogram
k Ω	kiloohm
m	metre
meV	millielectron-volt
mm	millimetre
neV	nanoelectron-volt
nm	nanometre
RAM	random access memory
rad	radian
S	siemens
s	second
sin	sine
μ eV	microelectron-volt
μ m	micrometre
μ S	microsiemens
Ω	ohm
$^{\circ}$ C	degree Celcius

Acknowledgements

I would like to express special appreciation and thanks to my supervisors Dr Konrad Walus and Dr Boris Stoeber. Your support, guidance, and patience helped me tremendously at all stages of my post-graduate work. I extend my sincere thanks also to Dr John Madden for providing feedback during the early stages of this work and serving on my defence committee. All three of you provided a tremendous amount of support for my education and research during both my undergraduate and post-graduate studies. You have granted me opportunities and insights that have been both unique and valuable.

I would also like to thank Henryk Modzelewski for his assistance with the computing cluster used to perform most of the simulations that drove this research and for reminding me that just because I sometimes get the results I expect does not mean they are necessarily correct.

Thank you to Shabnam Shambayati for her five rules to surviving grad school and to Sheng Pan for ensuring my workspace was always a good place to share adventure stories. May you live in interesting times.

Without the support of Arwen, Theo, Tess, Dylan, and Sara this might never have happened. Thank you.

Dedication

Engineering is only as useful as those it serves. While this endeavour was intellectually intriguing in a direct way, it also positioned me to build many of the new relationships that now fuel me emotionally. This work is dedicated to those who have fuelled me and helped me better serve.

Foremost: Tess Baker, Sara Pour, Mark Abbott, and Sean McHugh.

What next?

Chapter 1

Background

Electrically conductive composites can be created through the dispersion of conductive filler particles throughout an insulating matrix. Potential filler particles include carbon allotropes such as carbon black or nanotubes; organic conductors such as polypyrrole; and metals. Charge flow within these conductive composites has been attributed to a variety of transport mechanisms. A definitive trend shared by all the composites is that a composite with very little conductive filler has a conductivity near that of the insulating material and the conductivity increases toward that of the conductive filler as the filler is added. The current theory describing the physics that drive that conductivity change are explored further in the following sections.

1.1 Percolation

In the simplest case, conduction can be said to follow basic percolation theory whereby particles must touch in order for charge transport to occur [14, 15]. Net conductivity is then dependent on the total number of physically connected pathways between test points. At low loading volumes of conductive particles the mean distance between filler particles is large and the conductance of the composite is near that of the insulating matrix. As the volume loading of conductive particles, ϕ , is increased, the mean distance between filler particles decreases and they begin to form linkages. As linkages are sufficiently formed to create a conductive pathway through the matrix the conductivity of the particles begins to contribute to the conductivity of the bulk. At a critical loading fraction, ϕ_c , there is a sharp increase in conductivity, σ , as the conductive pathways reach sufficient abundance as to be common-place [16].

The critical loading fraction in a simple model such as this can be calculated statistically. A random filling routine is used to place particles in three-dimensional space. The critical loading fraction is taken to be the mean loading fraction at which 50% of these models exhibit a percolating cluster [4]. At this critical loading fraction, the material is said to be at its percolation threshold. At loadings near the critical loading fraction, the

conductivity can change drastically (over several order of magnitude) with small changes in the loading fraction [14, 16]. This simple percolation-style conductivity model follows a power-law behaviour of the form

$$\sigma \propto (\phi_c - \phi)^{-t}, \quad (1.1)$$

where t is the critical exponent and $\phi < \phi_c$. A continued increase in ϕ beyond ϕ_c results in a gradual plateau of σ that approaches the bulk conductivity of the filler particle. This gradual plateau also continues the power-law behaviour but with some signs reversed.

$$\sigma \propto (\phi - \phi_c)^t, \quad (1.2)$$

where $\phi > \phi_c$. The shape of this generalised relationship is shown in Figure 1.1. Simple percolation theory predicts a volume loading fraction of $\phi_c = 0.16$ and $t = 2.0$ for spheres packed cubically in 3D space and is not dependent on the size of the spheres or the size of the volume being considered [14, 17].

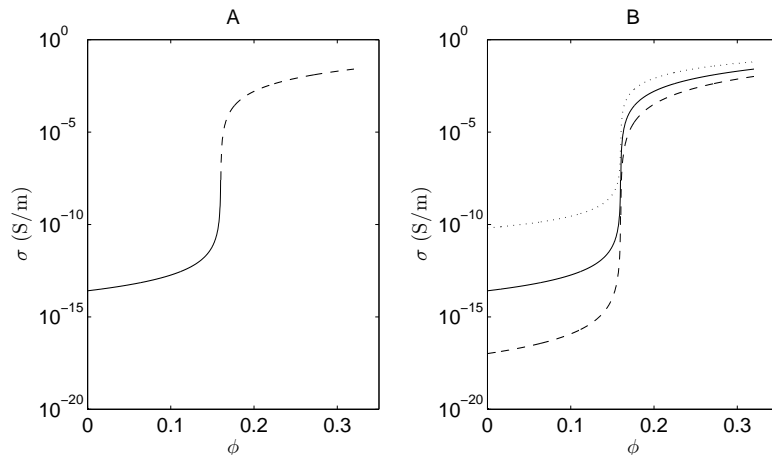


Figure 1.1: Figure 1.1A is an illustration showing the basic power law relationship described by combining equation (1.1) (solid line) and equation (1.2) (dashed line). In this illustration $\phi_c = 0.16$ and $t = 2.0$ are used and σ is scaled for visual clarity. Figure 1.1B does not differentiate between equation (1.1) and equation (1.2) but shows the effect of scaling t . For the dotted line $t = 1.5$, for solid line $t = 2$, and for the dashed line $t = 2.5$.

When experimental data is reviewed the simple percolation theory is quickly shown to be insufficient. Empirical analysis gives a critical exponent in the range of $t = 1.3$ to $t = 20$ [18–22]. There are conflicting views on

which physical properties influence which variables. Balberg, working with carbon black in polyethylene, claims ϕ_c and t are systematically related to the structure of the carbon black under test, as well as the moulding conditions [17]. Lower structure (more spherical) results in higher t values. As structure becomes higher (less spherical), t approaches a value of 2.0. This is attributed to the particle contact requirement of the simple percolation theory [17]. Others [14, 16] claim ϕ_c of the composite depends on the shape of the particles and the homogeneity of the dispersion while the critical exponent t depends on the material combination. Low values of ϕ_c have also been attributed to the formation of long conductive filaments and other inhomogeneities in the filler distribution [18]. Some [16, 23, 24] have made the specific claim that t values are not at all correlated to particle shape or ϕ_c .

Clearly there is a lack of consensus as one moves from the purely theoretical model involving perfect spheres in stochastically predictable arrangements to laboratory devices involving irregular shapes, sizes, and distributions. Much of this discord is rooted in the range of conduction influencers in situations where the particles seem unlikely to always be in contact. In these cases we turn to quantum tunnelling for additional insight.

1.2 Tunnelling conduction

1.2.1 Sphere to sphere tunnelling

When the dispersed particles are very small or have high aspect ratios, significant conduction is observed at volume loadings lower than the percolation threshold predicted by basic percolation theory. This is often attributed to a quantum tunnelling conduction mechanism whereby particles need not be in physical contact for charge transport to occur. The amount of charge transported between conductors that are not in contact falls off exponentially as the distance, δ , between them increases and is typically considered negligible between conductors more than $\delta = 10$ nm apart [16]. Despite this general consensus, there are published findings of tunnelling conduction occurring over gaps as large as $2.5 \mu\text{m}$ [25].

The amount of charge transported is also heavily dependent on the height of the potential barrier that occurs at the insulator-conductor junction. The potential barrier height, φ , between adjacent particles in composites comprised of a metallic conductor and a polymeric insulator is typically in the range $0.05 \text{ eV} > \varphi > 1 \text{ eV}$ [1].

The resistance, R_δ , between two sites is often given as

$$R_\delta = \frac{16\pi^2\hbar\delta}{3A\gamma q_e^2} e^{\gamma\delta}, \quad (1.3)$$

where

$$\gamma = \frac{2}{\hbar} \sqrt{2m_e\varphi}, \quad (1.4)$$

\hbar is the reduced Planck constant, A is the effective cross-sectional area where tunnelling occurs (between spherical particles), and q_e and m_e are the charge and mass of an electron respectively [2, 26]. In these analyses δ is generalised as the typical distance between particles in a large system with many parallel branches. A plot of equation 1.3 is shown in Figure 1.2. It is apparent that for the φ values being considered particles must be very close in order to register a meaningful conductance between them. Although the development of this equation describes A as the effective cross-sectional area where tunnelling occurs between spherical particles, a rigorous definition of “effective cross-sectional area” is not provided. The tunnelling conductance between spheres is going to be different than the tunnelling conductance between parallel plates of the same surface area (or projection area). A 1963 analysis of inter-particle conduction [27–30] that leads to equation (1.3) is typically at the root of modern analyses of this topic in the literature. The equation is of the same form as seen in analyses of scanning tunnelling microscopy although in those analyses a parallel plate assumption is typically either explicit or implied, even when tunnelling is occurring from a monoatomic needle tip. Point-to-point tunnelling approximations result in a neglecting of the terms $\frac{\delta}{A\gamma}$ (as is done later in equation (3.3)) [31–33]. These discrepancies in geometry assumptions nevertheless remain unresolved.

γ is defined from first principles as a description of wave function decay within the tunnelling barrier. The tunnelling barrier is dependent on the effective local work function [33]. An intuitive way to consider γ^{-1} is to treat it as a number representative of the distance over which tunnelling occurs (equivalent to exploring the case where $\delta\gamma = 1$). The location of γ in the exponential (1.3) gives it the units m^{-1} in agreement with the description in (1.4). Figure 1.3 shows the relationship described by equation (1.4) but inverts γ to better serve its consideration as an indicator of tunnelling distance.

As can be extracted from the line in Figure 1.3, the typical boundary values for φ stated earlier, 0.05 eV and 1 eV, give values for γ^{-1} of 0.437 nm and 0.0976 nm respectively. Despite the agreement of units, the values obtained seem too small to be a literal representation of typical tunnelling

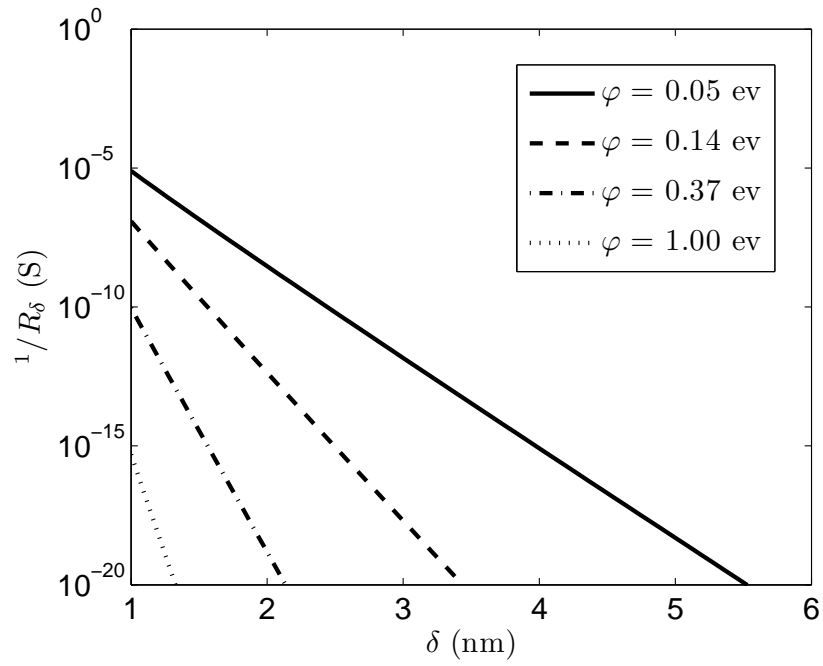


Figure 1.2: Equation 1.3 is represented by $\frac{1}{R_\delta}$ as a function of δ with lines shown for four different values of φ . In this example $A = \pi(10 \text{ nm})^2$.

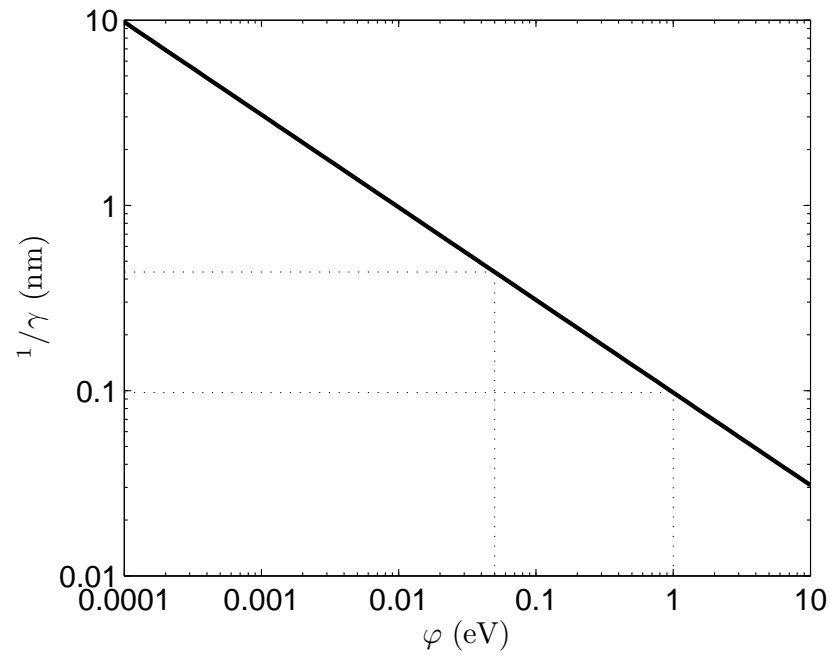


Figure 1.3: Comparison of potential barrier height and the constant γ according to equation (1.4). Recall that potential barriers in conductive composites are typically in the range $0.05 \text{ eV} > \varphi > 1 \text{ eV}$ [1]. The boundaries of that range are illustrated with dotted lines for reference.

distances. For reference, scanning tunnelling microscopy typically operates over a distance of 0.7 nm to 0.3 nm, equivalent in this analysis to a barrier height range of 0.02 eV to 0.1 eV [33, 34]. There is only a small amount of overlap in those ranges suggesting a direct comparison between γ and tunnelling distance may not be always fair. Nevertheless, this definition does offer a starting point for a model that requires a value for γ when mapping connections between particles.

Numerical values for φ and δ are not typically available for a prepared sample of conductive composite. In some cases they are treated as constants useful for fitting a trend line to experimental results. This approach is used by Wang *et al.* [2] in a composite of polydimethylsiloxane and carbon black where a unitless combined value of $\gamma\delta = 1.786$ is used to fit a trend line. Combining (1.4) with this definition gives the equality

$$\gamma\delta = \frac{2}{\hbar}\sqrt{2m_e\varphi}\delta = 1.786. \quad (1.5)$$

Solving for distance as a function of barrier height we find

$$\delta(\varphi) = \frac{1.786\hbar}{2\sqrt{2m_e\varphi}} \approx \frac{0.1743}{\sqrt{\varphi}}, \quad (1.6)$$

for δ in nm and φ in eV. Presumably the barrier height is relatively fixed within any single device but this relationship gives a range of possible values within which Wang claims his device operates.

An alternative way to experimentally determine values for φ and δ is by measuring the frequency response of a tunnelling device. Treating the device as a simple Resistor-Capacitor circuit, the dominant resonant frequency can be used to extract a mathematical description of the typical distance between the particles that are transporting charge. Resistance of the circuit is taken to be the one described in equation (1.3). The capacitance between any two particles, C_δ , is described by

$$C_\delta = \epsilon\epsilon_0\frac{A}{\delta}, \quad (1.7)$$

where ϵ_0 is the permittivity of free space and ϵ is the relative permittivity of the insulator. A capacitance equation of this form describes the capability of parallel plates to store charge. In the present examination the equation is assumed to approximately hold for semi-spherical plates in order to consider previous work in this field [3]. Capacitance and resistance can be combined to describe the resonant frequency,

$$f_0 = \frac{1}{2\pi R_\delta C_\delta}, \quad (1.8)$$

of the device in Hz. Substitute (1.3) and (1.7) into (1.8).

$$f_0 = \frac{3\gamma q_e^2}{32\pi^3 \hbar \epsilon \epsilon_0} e^{-\gamma\delta}, \quad (1.9)$$

where γ is defined by (1.4). Solve for δ as a function of γ .

$$\delta = \frac{\ln\left(\frac{3\gamma q_e^2}{32\pi^3 f_0 \hbar \epsilon \epsilon_0}\right)}{\gamma}. \quad (1.10)$$

This analysis method is used by Meier *et al.* [3] to consider a composite of polystyrenebutadiene and carbon black and results in the relationship

$$\delta(\varphi) \approx \frac{\ln \varphi + 43.5}{20.5\sqrt{\varphi}}, \quad (1.11)$$

for δ in nm and φ in eV.

Whereas [2] fixed the relationship $\gamma\delta = 1.786$ in equation (1.6), $\gamma\delta$ effectively ranges from 19.46 to 21.8 in equation (1.11) using data from [3]. In Figure 1.4 equation (1.11) is compared to equation (1.6) to gain further perspective on the barrier height vs tunnelling gap relationship extracted from the work of [2] and [3].

The results from [3] suggest typical distances between particles that are substantially further apart than the results from [2]. These extremes of the data in Figure 1.4 are summarised in Table 1.1. The δ ranges differ by a factor of 10. This serves to further illustrate the disagreement among researchers regarding typical properties of conductive composites.

φ (eV)	1	0.01	Data source
δ (nm)	0.17	1.7	Wang <i>et al.</i> (2010) [2]
δ (nm)	2.1	19.0	Meier <i>et al.</i> (2007) [3]

Table 1.1: Comparison of values for φ and δ .

In both sets of results, there must be very small potential barriers ($\varphi < 0.01$ eV) for devices where particles are typically more than 20 nm apart.

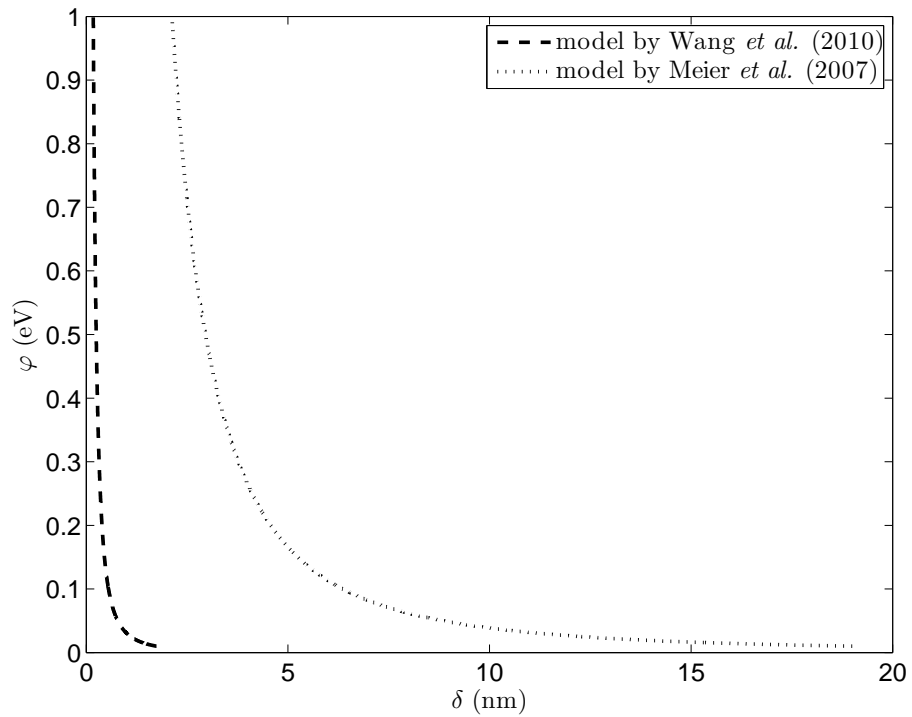


Figure 1.4: Comparison of potential barrier height (φ) and the inter-particle gap over which tunnelling must typically occur (δ) using the modelling approach from Wang *et al.* [2] and Meier *et al.* [3].

1.2.2 Hard/soft shell approach

In the case of small particles [15] or generally spherical particles with high aspect ratio tendrils [35], it can be instructive to consider the particles as hard solid spheres that have a soft outer shell. The hard solid cores behave as in the typical percolation model. They are incompressible and have a fixed ability to conduct when in contact with another particle. The soft outer shell defines an effective radius of interaction. If two particles under consideration have overlapping soft shells, they are considered capable of transporting charge. In a simplified model, this conduction can be considered to behave in an on/off fashion where only spheres with an overlapping soft shell need be considered. In this case the critical distance, δ_c , is the largest distance (core surface to core surface) that must be considered in order for a conducting cluster to span the sample 50% of the time [36].

Ambrosetti *et al.* [16] use this model at length and offer the resistance equation

$$R_\delta = R_0 e^{\frac{2\delta_c}{\xi}}, \quad (1.12)$$

where R_0 is a constant and ξ is a characteristic tunnelling length. Comparing equations (1.3) and (1.12) another relationship is apparent.

$$\xi = \frac{2}{\gamma}, \quad (1.13)$$

or, substituting (1.4),

$$\xi(\varphi) = \frac{\hbar}{\sqrt{2m_e\varphi}}. \quad (1.14)$$

This gives two opportunities to interpret physical meaning when γ , φ , or ξ is used as a fitting constant during the analysis of experimental data. A value for any of them suggests both a characteristic tunnelling length and a characteristic potential barrier height. Using (1.14) with the previous employed reference barrier heights yields $\xi(0.05 \text{ eV}) \approx 0.873 \text{ nm}$ and $\xi(1 \text{ eV}) \approx 0.1952 \text{ nm}$. The expression (1.13) results in exactly twice the values shown in Figure 1.3 and implies the relationship $\delta\gamma = 2$. As before the reference barrier heights are not in agreement with expected inter-particle distances.

The work done by Heyes *et al.* employs a series of Monte Carlo and molecular dynamics simulations to produce a set of equations that describe percolation events when randomly packing spheres using the soft shell and solid core approach to modelling [4]. Ultimately this results in a high order equation for critical distance with extremely good fit over the range $0.25 \times$

$10^{-7} < \phi < 0.62$ and normalised to particle solid core diameter (expressed here as $2r$). The critical distance is defined as

$$\frac{\delta_c}{2r} = 1 + \frac{1}{f(\phi)}, \quad (1.15)$$

and illustrated in Figure 1.5 using

$$f(\phi) = (a_0\phi)^{\frac{1}{3}} + (a_0\phi)^{\frac{2}{3}} + (a_0\phi) + \frac{4}{3}(a_0\phi)^{\frac{4}{3}} + \frac{5}{3}(a_0\phi)^{\frac{5}{3}} + 2(a_0\phi)^2 + a_1\phi^3 + a_2\phi^4 + a_3\phi^6, \quad (1.16)$$

where $a_0 = 2.8902$, $a_1 = 129.644$, $a_2 = -98.334$, and $a_3 = 1302.40$ [4].

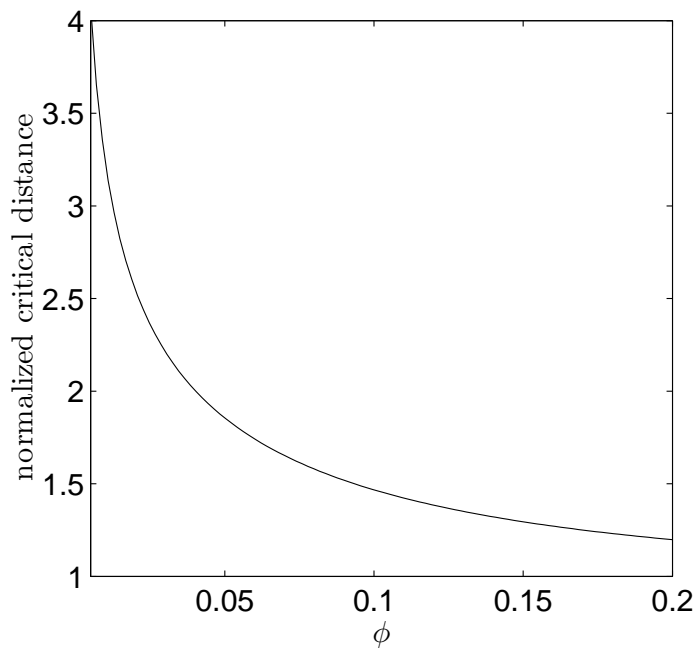


Figure 1.5: The normalised critical distance, $\frac{\delta_c}{2r}$, is shown with respect to volume loading fraction of solid core spheres. The relationship is described explicitly by equations (1.15) and (1.16) taken from [4].

The random packing approach to the development of this model is instructive as the numerical outcomes reinforce the notion that random packing is unlikely to be taking place during the mixing and curing of conductive particles in an insulating polymer matrix. Solving equation (1.15) for

$\phi = 0.05$ and $r = 25$ nm yields a critical distance of about 90 nm or, using equations (1.12) and (1.14), the tunnelling barrier is on the order of 20 μeV . If the typical radius is increased to 65 nm, the critical distance and tunnelling barrier change to about 240 nm and 4 μeV respectively. It is not typically reasonable to expect tunnelling to occur over distances that large nevertheless composites prepared at those loadings and particle sizes have been shown to exhibit conductivity [8, 37]. An apparent conclusion is that this simple model makes assumptions that are either not valid or fail to account for something in those experiments. The model requires further refinement.

1.3 Particle agglomeration and filament formation

An analysis of carbon black in poly(methyl methacrylate) has revealed that the particles formed wire-like structures with wire diameters as small as 24 to 31 nm and edge lengths over 1 μm [38]. This work reveals a distinctly Voronoi-like structure. Samples were prepared using carbon black with a mean diameter of 21 nm. Final preparation employed a press sinter method that squeezes the sample during curing. The cured material is then thinly sliced and imaged. A figure of merit in this work is the ratio of filler particle size to wire diameter. This suggests it is reasonable for wire-like filaments to form that may be only slightly thicker than the mean diameter of their constituent particles [38]. Scanning electron microscopy of carbon black with a mode diameter near 50 nm in polyethylene and polypropylene is in general agreement, showing filaments and Voronoi cell-like structures with cell edges on the order of several μm long and filaments with variable diameters from less than 0.2 μm to greater than 1 μm [39].

1.4 Carbon black as a conductive filler

Carbon black is most commonly manufactured by combustion of heavy oils. The carbon precipitates out as small particles. The small particles fuse to form aggregates. Large aggregates tend to have more structure (be less spherical) with a substantial number of branches. The high surface area promotes conduction and promotes situations where aggregates, influenced by Van der Waals forces, cluster together into larger groups called agglomerates [8]. Carbon black can also begin as carbon pellets that are sheared and crushed to form smaller particles. During the shearing and crushing

process carbon black again aggregates and agglomerates because of interactions between particle surfaces [40, 41]. In both cases, this aggregated state typically results during the manufacturing process. Aggregates in mixture with a rubbery matrix tend to further coalesce to form larger agglomerates. During mixing it is believed that agglomerates often break apart and re-form but aggregates remain substantially unchanged [5]. A scattering profile study of carbon black before and after combination with polymers shows that the smallest size of carbon black agglomerates grows during the mixing and curing process suggesting that the carbon black has bonded into filaments bounded by polymer chains [42]. The size and shapes of the new carbon black units depends on the polymer, the mixing conditions, and the curing conditions [5, 8, 42–46].

It is common to describe the behaviour of carbon black conductive composites using a percolation model, a tunnelling model, or a combination of the two. The two models are limited in their compatibility and still fail to explain the myriad differences in experimental results. The most substantive incompatibilities stem from the requirement that in a tunnelling model particles must be within a few nanometres of each other yet must not touch while they must form a geometric continuum for percolation to occur. While there is consensus that the conductivity of a particular carbon black-polymer composite will vary as the volume loading of carbon black, it has also been noted that changing the type, and therefore the carbon black particle structure and size, may also yield very different conductivity despite a constant volume loading. Those same geometric differences also affect tunnelling performance as high aspect ratio geometries can lead to large electric fields that distort the tunnelling barrier potential profile and result in augmented quantum tunnelling. Work done by Verhelst reveals this variation in the extreme. Five different carbon blacks (with mean diameters of 30 nm, 10 nm, 29 nm, 42 nm, and 29 nm) are mixed with polystyrene-butadiene. The test samples exhibit very different percolation curves and require different volume loadings (10.4%, 19.1%, 28.7%, 43.3%, and 53.1% respectively) to achieve the same resistivity (about 7.4 k Ω m) [46]. In general qualitative terms this means that particle structure and size must be captured in any analytical model either directly or, more often, indirectly within fitting constants such as a unique percolation threshold, percolation critical exponent, and potential barrier height for each combination of a type of carbon black, a polymer, and possibly also each set of mixing conditions.

There is agreement among scientists that, for a fixed volume loading, the presence of smaller agglomerates enables a more favourable distribution of particles with smaller inter-particle distances [1, 8, 45]. This increases

the likelihood of charge transfer through the insulating barriers between particles.

Absolute minimal inter-particle distances are suggested by some of the chemical properties of carbon. The length of a carbon to carbon bond is 0.14 nm and the inter-planar spacing of graphene sheets in graphite is 0.34 nm [47]. It has been shown that as loading increases, the distance between particle cluster centres decreases but the distance between particle cluster edges approaches a threshold value near 3 nm [5]. This result is shown in Figure 1.6 [5]. An implication of this and the acknowledgement that agglomerates both break apart and form during the mixing process is that aggregates closer than 3 nm tend to fuse into agglomerates and that freshly broken agglomerates tend to separate by at about 3 nm.

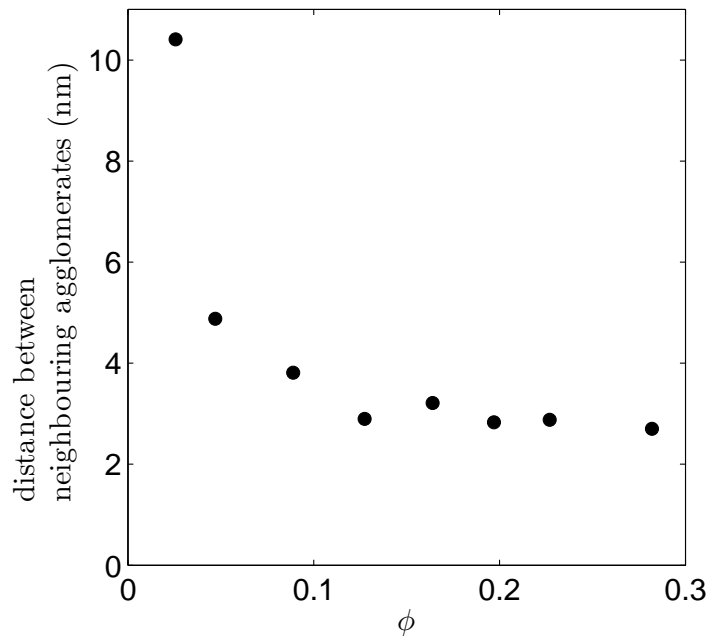


Figure 1.6: Typical distance between nearest-neighbour carbon black agglomerates in natural rubber as a function of volume loading fraction. Adapted from [5].

One of the most popular forms of carbon black used for creating conductive composites is Vulcan XC72 made by Cabot Inc [48]. A scanning electron microscope micrograph of Vulcan XC72 is shown in Figure 1.7.

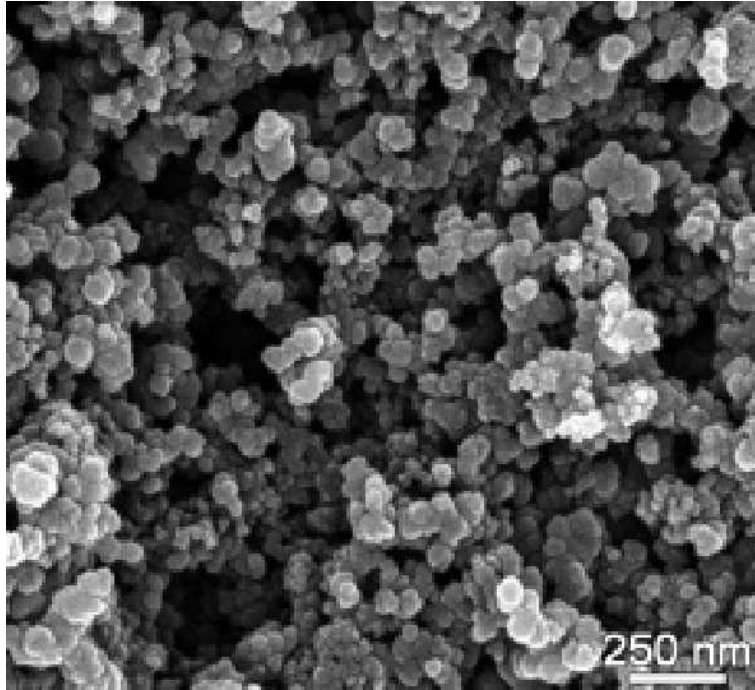


Figure 1.7: Scanning electron microscope micrograph of Vulcan XC72. Reprinted from [6] with permission from Elsevier.

Figure 1.8 contains data points from experimental works done across a range of loadings of two different carbon blacks in four different polymers. These results will serve as a reference for results produced during simulation. The second carbon black, Black Pearls 2000, is also produced by Cabot Inc.

Size profiles of Vulcan XC72 done by the author, a colleague [9], and others suggests a log-normal distribution of particle diameters [37, 46, 49, 50]. Spectroscopy measurements and scanning electron microscope measurements of particles tend to differ in conclusion regarding the most abundant unit size. Spectroscopy measurements tend to give a diameter ranging from 100 nm (in water with a surfactant) [9] to 400 nm (in oil) [50] whereas scanning electron microscope analysis of pure carbon black suggests a diameter range from 30 nm to 125 nm with a mode diameter near 55 nm [11, 37, 46, 49]. A spectroscopic analysis of the material shown in Figure 1.7 (and published with that image) suggests a mode diameter in excess of 300 nm in clear contradiction with the image in Figure 1.7 [6]. Liu *et al.* examined transmission electron microscope images of carbon black that had been applied in suspension to a substrate and then allowed to dry. The resultant size profile is shown in Figure 1.9. This supports the notion that particles in suspension are forming agglomerates much larger than the size of any single particle or aggregate [13].

Despite this potential confusion there is consensus in the assertion that the particles have a high degree of structure and are prone to aggregation and agglomeration so it may be reasonable to attribute some of this difference in size measurement results to agglomeration within the dispersal medium used for spectroscopy. Studies of Vulcan XC72 cluster size done after mixing and curing support claims that within a rubbery matrix aggregates on the order of 100 nm to 150 nm are typical and they readily join to form larger agglomerates [5, 39].

For the purpose of modelling, Vulcan XC72 at a loading of 3% by volume is used as a starting reference as it is a volume loading that shows measurable conductivity in published works and the particle size distributions for Vulcan XC72 are reasonably well described. A typical diameter near 125 nm is assumed for small aggregates: some aggregation is assumed to have taken place with the expectation that the algorithms used to model particle arrangement will capture agglomeration phenomenon.

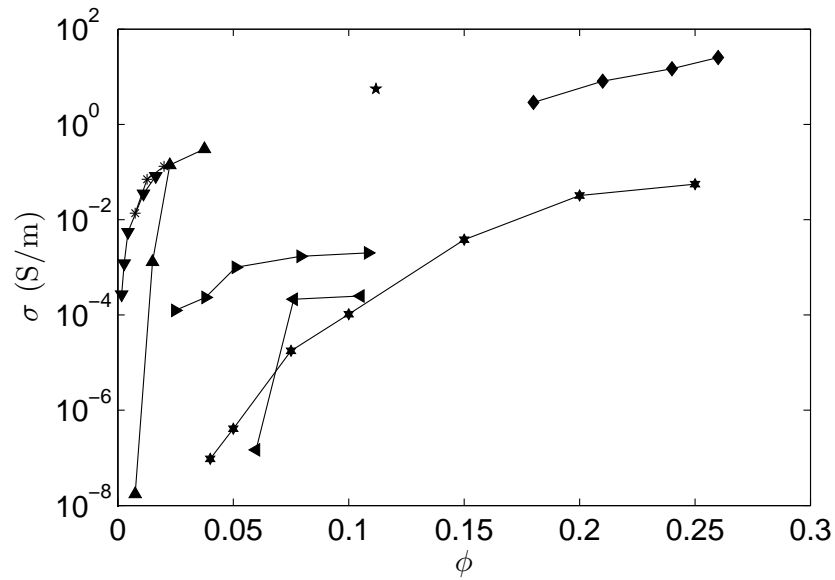
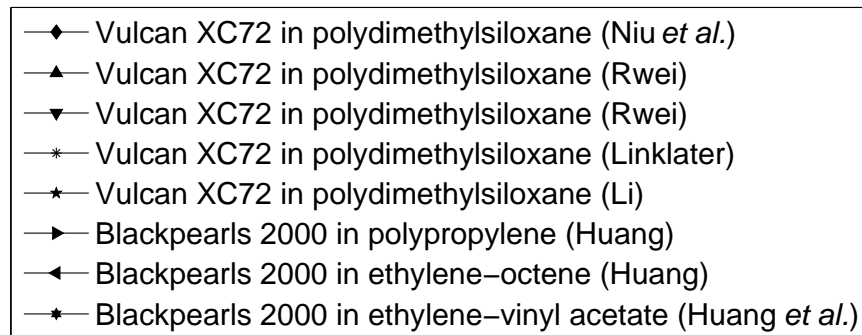


Figure 1.8: Conductivity across a range of loadings of two different carbon blacks in four different polymers. Taken from works published or shared by Niu *et al.* [7], Rwei *et al.* [8], Linklater [9], Li [10], Huang [11], and Huang *et al.* [12].

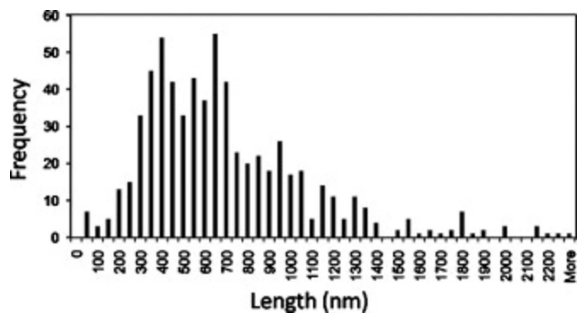


Figure 1.9: Size distribution of Vulcan XC72. Data represents about 660 particles in about 200 images. Figure created by [13]. Reprinted by permission of The Electrochemical Society.

1.5 Summary

Prior work has shown that a combination of percolation and quantum tunnelling effects must be considered in order to successfully model the internal behaviour of conductive composites. While the physics of individual components seem reasonably well understood in isolation there remains some ambiguity with respect to the combined effects as well as their interaction effects. Carbon black has been demonstrated as a useful conductive filler, but characterisations of the filler are inconsistent.

In general, a successful model must allow for variability in particle size, incorporate agglomeration effects and filament formation, and account for conduction due to both contact and tunnelling. The following sections outline the modelling approach used and review the mathematics and physics that drive the model. Modelling results are then presented and discussed. Finally some thoughts are presented for future work that could serve to move this model forward or otherwise improve the work described herein.

Chapter 2

Experimental methods

Modelling experiments were conducted using software written in MATLAB and executed on a dedicated high performance computing cluster. The cluster consists of 20 Dell PowerEdge 1950 servers each with a pair of 2.66 GHz quad core Xeon processors and between 8 and 32 GB of RAM.

In order to approximate the random nature of physical mixing and variation in particle size, several randomization algorithms were created with parameters tuned semi-empirically. A pass in the simulator typically involved six steps: load or generate all needed model parameters and establish model boundaries, place particles and electrodes according to a set of predefined rules, create a map describing the connections to and from all particles within one radius of interaction of each other, calculate the inter-particle conductivity for each connection, calculate the bulk equivalent conductivity of the model, and finally store or present the results in data files or figures. This is diagrammed in Figure 2.1.

The first and final steps are reasonably simple and computationally trivial. Particle placement methods are described in Section 2.1. Connections between particles are mapped by examining the space one radius of interaction from the surface of each particle. Using the language introduced in Section 1.2.2, it is a check to see if the soft shell of one particle reaches out as far as the hard shell of any other particles. The computation of inter-particle conductivity is relatively simple though the underlying physics of the calculation warrants analysis. This analysis is done in Section 3. The bulk conductivity calculation treats the system as a large resistor array and solves the system using nodal analysis. Computing the solution involves the inversion of a large matrix. If the resistor network does not complete a path from end-to-end or has only a weak end-to-end connection a conductivity of or near zero would be expected. This situation creates a singularity whose computation produces numerical values that are very small and may be positive or negative. Negative results are easy to identify as being errant but small positive values may be the result of either no connection or a very weak connection. The lower numerical limit of reliable simulation data presented herein is somewhere between 10^{-8} and 10^{-9} S/m. Alternately

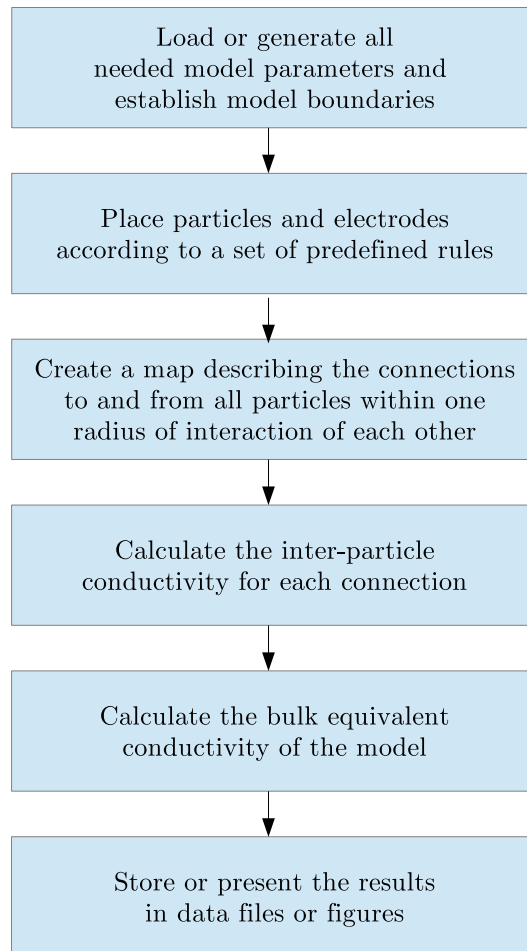


Figure 2.1: Processing the present model involves six steps that are described in the text.

put, an estimated numerical error of $\pm 10^{-8}$ S/m should be applied to all computational results presented herein.

2.1 Particle placement

Particles are placed in a semi-random fashion throughout a specified volume. Several different distribution algorithms were explored. Several of the methods are described below. All the methods approximate particle shape as a sphere of fixed radius. In some cases the spheres are of uniform size and in others cases there is a distribution of sizes.

2.1.1 Method 1: random placement of uniform particles

This is the most basic placement algorithm and is the foundation upon which the others are built. The number of particles needed, n , is calculated as

$$n = \frac{V\phi}{\frac{4}{3}\pi r^3}, \quad (2.1)$$

where r is the particle radius and V is the total volume being simulated. Particles are seeded by randomly assigning particle centre coordinates. A validity check then occurs to ensure a newly placed particle does not intersect an existing particle. Intersecting particles are deemed to be invalidly placed and are then removed. The process loops until all particles have been placed.

2.1.2 Method 2: clustering

Particles are generated as in placement Method 1 but the validity check has an extra component. In addition to avoiding intersections particles must, with a user defined probability, be within a user defined distance of any existing particle. This allows the user to approximate empirical observations of particle agglomeration [44] and tendency to form filaments [51]. In each successive modelling pass the algorithm is repeated for any particles that failed intersection related validity checks. This can result in slightly more randomly placed particles than defined by the user but allows a model whose other parameters are overly constrained to run to completion with the user then being informed of any resultant deviations from input parameters. A weakness of this approach is that computation time quickly becomes prohibitively long for small particles in large systems. This weakness was one of the motivations to explore other approaches that could produce similar

or better results. Further insight into this modelling methodology as well as some of the results it produced are presented in Section 4.4.

2.1.3 Method 3: volume exclusion method

Before seeding particles, spherical exclusion zones are created based on a user defined exclusion fraction and exclusion size. These two tunable parameters allow the user to approximate an empirical phenomenon whereby particles tend to create shell-like structures around areas that contain few or no particles [39]. This is generally attributed to surface effects [52, 53].

This methodology has been used by others to model the formation of carbon black filaments in rubbers [54]. The model created by Jean *et al.* was formulated and tested using imaged slices of composite material where the particles have a mean radius of 20 nm and the slices have a thickness of 40 nm (± 10 nm). During the extensive analysis of particle aggregation and agglomeration, conclusions are drawn regarding the structure of the particle distribution. It is noted that a Voronoi tessellation is well suited to this type of modelling although a volume exclusion methodology is then pursued to approximate the structure. The authors show that while the carbon black particles are spherical and take on a log-normal distribution of sizes, they form aggregates that can be considered spheroids and are about ten times as large as their constituent particles. The authors use these spheroidal approximations of aggregates to create a suitable set of spherical exclusion zones within which no particles may exist. Spherical particles are then randomly placed within all space except that defined by the exclusion zones. Parameters such as the size and density of these zones are tuned by an automated process that compares slices of the resultant 3D space with images of the material slices until the particle and aggregate shapes and densities match to within a pre-set confidence interval [54]. Despite this effort, the presented model still fails in two notable ways. It does not offer meaningful insight into the volume resistivity of composites modelled and the model does not survive scaling (it percolates less as the model scales up). The former may be an oversight on the part of the authors as they do present resistivity data for their reference material but the latter is clearly an area for improvement as the usefulness of their model is surely tied to its ability to predict the behaviour of increasingly larger volumes of material.

Within the present work a volume exclusion modelling method was implemented as per the following. Uniform particles were generated as in placement Method 1, however, particles were allowed to fall within an excluded zone with a user defined probability. The probability of being allowed

within an exclusion zone or not was included as a user tunable variable in order to more closely approximate empirical results. This does not affect volume loading fractions but increases the likelihood of particles being nearer to one another. A two dimensional representation of this approach is shown in Figure 2.2. This method yielded results in some cases that were similar to the shell and filament effects described in published works [5, 39, 44, 51–53], however the computation time for the simulations became prohibitively long.

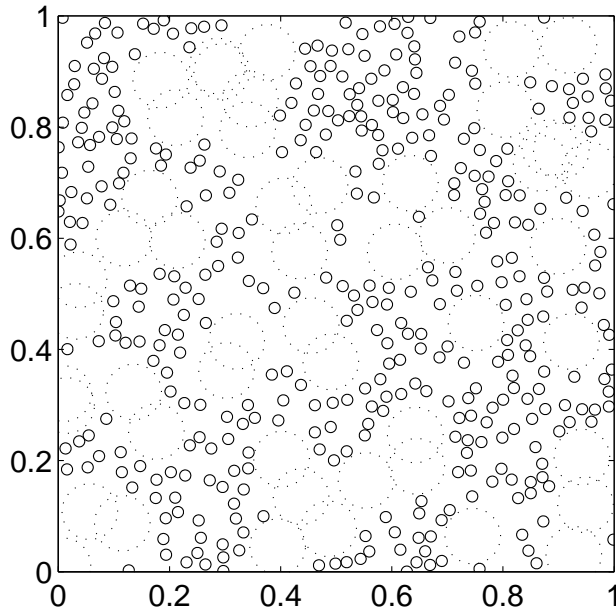


Figure 2.2: A two dimensional arbitrary unit representation of the volume exclusion method described in Section 2.1.3. Exclusion zones are shown as circles with a dashed line (radius = 0.05). Particles are shown as a circle with a solid line (radius = 0.01). In this example, exclusions zones are permitted to overlap, particles are not, and no particles may be in an exclusion zone.

2.1.4 Method 4: Voronoi wire frame method

The wire frame method seeks to improve on the filamentation results of placement Method 3 while simultaneously reducing the computation time involved in creating and analysing the model. Rather than creating exclusion

zones as a sphere using a centre point and radius, which must then be compared to every particle placed to check for intersection, exclusion zones are only defined as a point. The array of exclusion points is used to generate a three dimensional Voronoi structure wire-frame in the modelling space where the particles are placed on the “wires”.

A Voronoi diagram divides space using boundaries drawn between seed points such that only one seed point is enclosed within each region. All space within each region is closer to its own enclosed seed point than it is to any other seed point. In two dimensions this is relatively easy to visualize and is shown in Figure 2.3. This style of geometry is consistent with observations of natural phenomenon such as polycrystalline micro-structures in metallic alloys [55–57]. It is also used in a variety of mapping applications [57, 58].

In three dimensional space the principle is the same but the product is visually more complex. Rather than a map of convex polygons that enclose seed points in a two dimensional plane, the map is instead divided into convex polyhedra that enclose seed points in three dimensional space [57]. To aid in visualization an example 3D Voronoi structure is presented in Figure 2.4 as a stereographic image set.

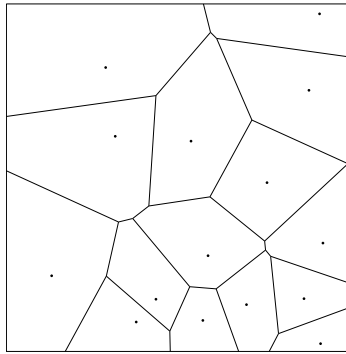


Figure 2.3: A 2D Voronoi structure with cell edges shown as lines and dots at each seed point.

Analyses of composite materials have shown Voronoi-like structures of carbon black throughout [5, 38, 51, 54]. Work by Jean *et al.* using carbon black in natural rubber revealed a characteristic Voronoi edge length of 96 nm to 128 nm, 5 - 6 times the size of the constituent particles (whose mean radius is given as 20 nm) [54]. Work by Levine *et al.* using carbon

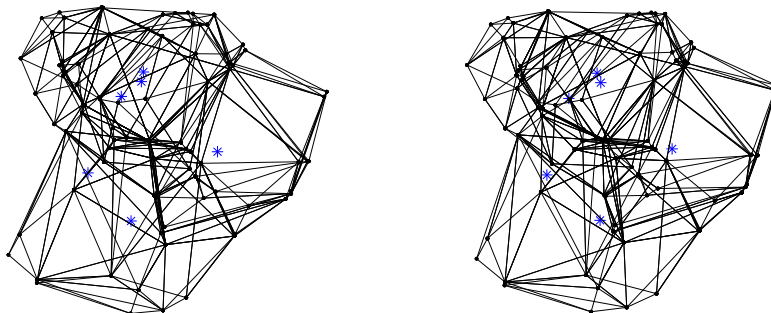


Figure 2.4: Stereographic example of a 3D Voronoi structure with cell edges shown as lines and dots at each vertex. Seed points are shown as a star. Hold image about 50 cm away and allow eyes to cross slightly. When three images appear, observe the central one.

black in poly(methyl methacrylate) measured unbroken wire segments up to 100 μm long and mean wire thickness less than ten times the size of the constituent particles (whose mean radius is given as 21 nm) [38]. These numbers serve as references when adjusting model parameters.

In the present model, seed points are randomly assigned. The volume and perimeter of each Voronoi cell is calculated. During particle placement, each particle is randomly assigned to either be placed anywhere in the model volume, or be placed within a user defined range of one of the Voronoi cell segments. Assignment to a particular segment is weighted to ensure all segment sections have equal probability of being selected for a particle, in other words, an equal probability per unit length. Finally, particles are checked for intersection.

2.1.5 Method 5: distributed radii

Particles were sized according to a log-normal distribution centred about published mode particle size values as described in the literature [6, 50, 54]. The mode size of the particles is preferred to the mean as the mode size identifies the most commonly occurring (or the typical) particle size but the two values differ for a log-normal distribution. During discussions of input parameters and output results a combination of mode and mean must how-

ever be used. This is because while “mode” is more useful when defining the type of distribution the randomization algorithm is to produce, it is not possible to directly calculate the mode of a discrete number of points each of which is drawn from a continuous distribution. In cases where a published size range was used as a reference the range values were treated as the 95% confidence intervals for the log-normal distribution. This combined mode and variance were set at execution time but they were permitted to drift. The drift would occur as a result of particles being rejected due to intersection. During each subsequent placement pass, new particles were generated using the same probability distribution function. Because there was a greater likelihood of larger particles experiencing intersections, the likelihood of having an abundance of smaller particles increased with each pass. Placement passes continued until the total required volume of particles was reached. An example of the output from this algorithm is shown in Figure 2.5. Using a log-normal distribution allowed particles to take on a random radius while maintaining non-negative values and favouring smaller particles over larger ones. This was deemed appropriate as mechanical mixing has been shown to break apart large agglomerates [5]. All simulations results presented herein include algorithms that create particles whose sizes are distributed in this way.

2.1.6 Method 6: intersections allowed

The placement methods described above all served to better approximate the formation of agglomerates, clusters, and filaments of particles described in literature [5, 44, 53]. They also improved the bulk connectivity of the model. The connectivity improved because the mean distance between particles decreased and particle networks became more likely to span the extent of the model. This accounts for connectivity between particles where a tunnelling or hopping type conduction mechanism is dominant but does not readily account for connectivity that might result if two particles were to be in physical contact. The placement algorithm, despite all the additional constraints introduced, still assigns a bounded random coordinate to each particle, a bounded random radius, and then ensures it does not intersect other particles. This results in a situation where the likelihood of two particles being in contact is approximately zero and, even if it were to occur, it would be a point-contact with no cross-sectional area and thus be unsuitable for conventional conductivity consideration. To approximate situations where particles may come into contact and stay in contact with each other, slight intersection of particles was allowed and the amount permissible was

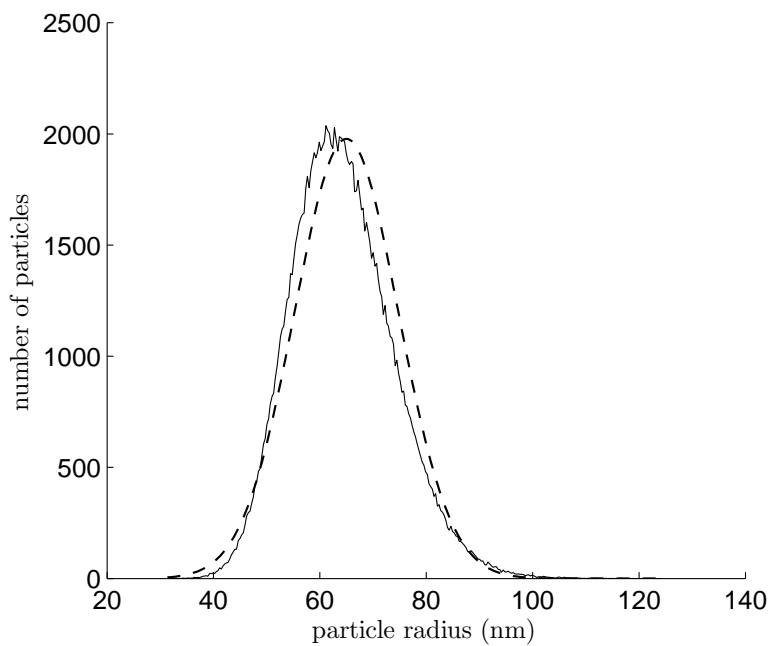


Figure 2.5: In this example set of particles the user set target mean radius and standard deviation were 65.0 nm and 9.75 nm respectively. A log-normal distribution with those parameters is shown as a dashed line for reference. It has a mode radius of about 62.8 nm. The resultant particles from four successive models are combined and histogram data of the resultant radius distribution is shown as the solid line. Histogram bins span about 0.32 nm. Particle radii vary from 31.2 nm to 124.5 nm with a mean and standard deviation of 64.3 nm and 9.55 nm respectively.

subject to user adjustment.

2.2 Particle connectivity mapping

Having placed all the particles using one of the methods described above, they must now be evaluated to determine their connectivity to each other particle being modelled. The degree of effective connectivity between particles is dependent on their proximity to one another. Two connectivity situations are considered. When particles are in direct contact with one another the notion that they are connected is obvious. A case requiring greater reflection occurs when particles are near one another but do not touch. As previously discussed in Section 1.2.2, one way to check for and model this type of connectivity is by defining particles as having a soft, permeable shell that surrounds a solid core [4, 59, 60]. If a soft shell touches a neighbouring solid core, particles are said to connect. Solid cores are not typically permitted to overlap. In a basic mathematical model this type of connectivity has a binary state: particles either connect or they do not; they either form a network or they do not. An alternate interpretation is to use this approach to check for connectivity but define the connection in quantum mechanical terms as a gap over which tunnelling occurs. The soft shells then define a radius of interaction where tunnelling conduction will be computed. The rule prohibiting hard shells from overlapping is relaxed in order to allow random placements that result in direct, classically conductive connections to occur within agglomerates.

Because tunnelling conduction falls off exponentially as tunnelling distance increases, there will be a threshold particle gap or soft shell size above which the amount of charge transport is negligible and particle connections can be said to be absent. Computationally it is practical to assign an upper bound on the distance worthy of consideration. Beyond that upper bound, called the radius of interaction, r_i , the amount of charge being transported is taken to be sufficiently negligible that it need not be considered.

In a model filled with randomly placed particles all potentially contributing to charge tunnelling or hopping it is conceivable that each particle transmits charge to or receives charge from every other particle. This is captured in a map that describes the distance between all particles. Particles that intersect and are therefore in direct contact will have a negative gap equal to the amount of linear overlap. Non-overlapping particles are considered as sites where tunnelling is occurring. As previously discussed, some of those charge flows will be negligible. The negligible flows can be identified by

their correspondingly large distance between particles allowing the map to be pruned to only include the particle connections spanning gaps less than the radius of interaction.

2.3 Electrodes

As the ultimate goal of the model is to represent a bulk material and approximate its end-to-end conductivity the model requires that consideration be given to electrodes. In physical embodiments the electrodes are typically a good conductor with physical properties that suit the associated experiment or application. Examples include conductive grease, evaporated metals, foil, and poly3,4-ethylenedioxythiophene/polystyrenesulfonate (a conductive polymer) [15, 22, 35].

In our model, electrodes are represented fundamentally the same as other conductive points but they have some special properties: they are geometrically confined to the planes of the electrodes, they have no thickness, and they are sufficiently abundant as to approximate a continuum. The first two criteria are absolute and the third is subjective. When modelling electrodes in this way there are two possible outcomes if the abundance of electrode sites is ill defined. If there are too few electrode sites it is likely that despite a possible internal network of particles there will be a lack of electrode connection sites within the radius of interaction of the particles in the bulk despite many particles being near the electrode plane. An example of this is shown in Figure 2.6A. This is analogous to an overly high contact resistance. If there are too many electrode sites, connections from the nearby internal particles will be very likely to occur and potentially over represent the connectivity. Figure 2.6B shows the same internal network as Figure 2.6A, but with an increased number of electrode sites. This is analogous to an overly low contact resistance. In this model the latter situation is favourable. An artificially low contact resistance ensures that the resistance of the bulk dominates.

In order to ensure good connectivity without creating an overwhelming number of electrode sites, electrode sites that do not connect with any bulk particles are removed before performing conduction calculations.

2.4 Node trimming

As the model requires computationally intense mathematics and the inversion of large matrices there is incentive to use the fewest number of electrical

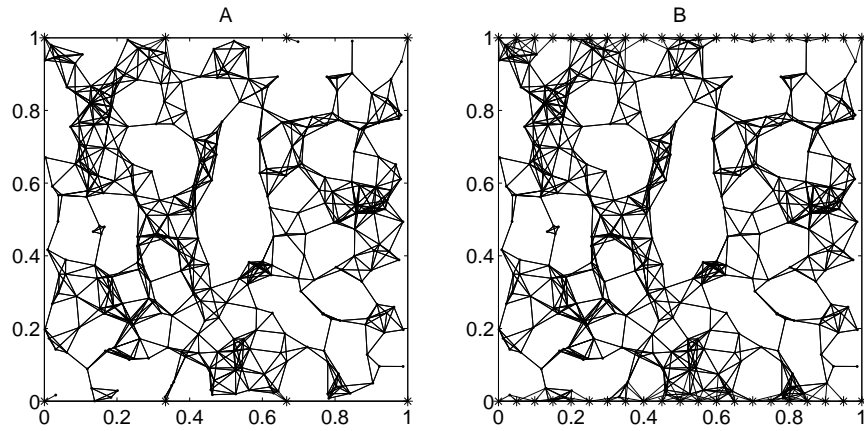


Figure 2.6: In this two dimensional arbitrary unit example conductive particles are shown as \cdot and electrodes are shown as $*$. Connections between sites (particles or electrodes) are shown as a line. Diagram A shows a connected network that has few electrode connection sites. Diagram B shows the same network but with more electrode connection sites. Observe the difference between the two diagrams in particular near x-axis locations 0.2, 0.5, and 0.8.

nodes possible. Each particle within the model will develop its own potential and participate in charge transport as long as it is either connected to at least two other particles or connected to one other particle and an electrode. Each electrode is composed of many particles without a radius and all its constituent particles are considered to be equipotential. One electrode is grounded and the other is held at a fixed voltage. These details allow the implementation of an algorithm for determining if any electrode sites can be ignored when tabulating the electrical nodes. Any particle without a connection to another particle is not considered an electrical node. Any particle with only one connection to another particle must also have a connection to an electrode or else it is not considered an electrical node. These particles that are marked as not being electrical nodes will be ignored during conductivity calculations. An example of this is shown in Figure 2.7.

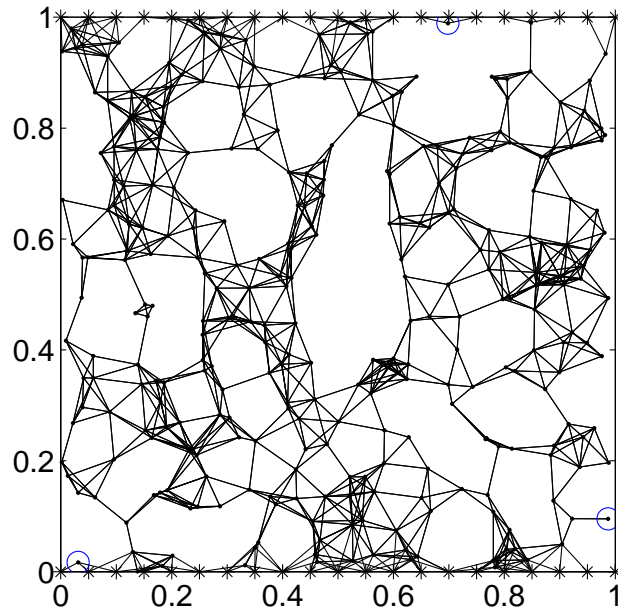


Figure 2.7: This two dimensional arbitrary unit example contains the same connected network as Figure 2.6B. Conductive particles are shown as \cdot and electrodes are shown as $*$. Connections between sites (particles or electrodes) are shown as a line. Three particle sites that do not contribute useful electrical nodes have been identified (with circles) as suitable for exclusion from the conductivity calculation.

Chapter 3

Inter-particle conductivity

Once the mapping of connected particles is complete and trimmed each connected pair is considered individually to determine the conductance between them. Particles may be in contact or have some distance between them. The present work developed a variety of methods used to model the charge transport occurring in conductive composites. The first method presented is very basic and the subsequent methods are more sophisticated.

3.1 Absolute path length

In the simplest of modelling situations a conductance, G , is assigned proportional to the linear distance between the particles.

$$G = \frac{\sigma_\delta}{\delta}, \quad (3.1)$$

where σ_δ is a conductivity parameter that describes the conductivity of a fixed cross section, and δ is the distance between the two particle surfaces. This method accounts solely for the empirical observation that as the mean distance between particles decreases, conductance increases. It does not consider any of the more complicated physics that contribute to conductivity. The computation time is very short and this method can be instructive when looking for general changes in the model due to alterations in input parameters such as geometry, particle size, and volume loading. It provides very little physical meaning but does offer insight into whether the number of end-to-end connections has increased or decreased due to a parameter change in the simulation.

3.2 Basic exponential

Using an exponential algorithm to calculate inter-particle conductance, G_t , approximates a tunnelling type of charge flow. The equation has the form

$$G_t = G_0 e^{-\gamma\delta} + G_1 \quad (3.2)$$

where G_0 is a base conductance and G_1 is the conductance of the insulating filler. The physical meaning of γ is explored in the definitions of equations (1.4) and (1.13). This relationship between conductance and distance is applied to all gaps greater than zero and less than the upper limit imposed by the radius of interaction and captures point-to-point charge tunnelling across the distance between particle edges without considering the cross section of the particles. Using this information G_0 is defined using (1.3) as a reference.

$$G_0 = \frac{3q_e^2}{16\pi^2\hbar}. \quad (3.3)$$

This gives $G_0 \approx 4.6 \mu\text{S}$.

Models that describe imaging systems such as scanning tunnelling microscopes successfully use this analytical approach for scanning tips with a radius of curvature less than 200 nm suggesting that this is a reasonable approach for models with particles sizes less than that limit [33].

3.3 Conduction due to particle contact

Conduction arising from particle contact is assumed to follow classical conduction theory. The amount of contact occurring is related to the amount the particles overlap in the model. The conductance in this area, G_c , is approximated as

$$G_c = \sigma_c \frac{A_c}{a}, \quad (3.4)$$

where σ_c is the internal conductivity of the conductive particles, A_c is the cross-section of the contact area, and a is the distance between sphere-centres.

$$A_c = \pi r_c^2, \quad (3.5)$$

where r_c is the radius of the contact circle made by the two overlapping spheres. From Figure 3.1 the distance between sphere-centres is

$$a = r_1 + r_2 + \delta, \quad (3.6)$$

where r_1 and r_2 are the respective radii for the two spheres being considered.

The angle between the point of overlap and the straight line between centres is shown as angle θ . The law of cosines is used to describe the relationship between these lines and θ ,

$$r_2^2 = r_1^2 + a^2 - 2r_1 a \cos(\theta). \quad (3.7)$$

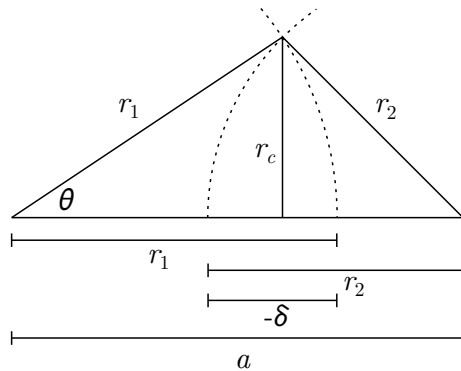


Figure 3.1: Geometry between overlapping spheres, $\delta < 0$. When $\delta > 0$, $r_c = 0$, and the spheres do not overlap.

This can be rearranged to find

$$\theta = \cos^{-1} \left(\frac{r_1^2 - r_2^2 + a^2}{2r_1 a} \right). \quad (3.8)$$

The contact radius,

$$r_c = r_1 \sin(\theta), \quad (3.9)$$

is found as a function of θ through trigonometry. Substituting (3.6) and (3.8) into (3.9) gives

$$r_c = r_1 \sin \left(\cos^{-1} \left(\frac{r_1^2 - r_2^2 + (r_1 + r_2 + \delta)^2}{2r_1(r_1 + r_2 + \delta)} \right) \right), \quad (3.10)$$

for $\delta < 0$.

Substituting (3.5) and (3.6) into (3.4) produces

$$G_c = \frac{\sigma_c \pi r_c^2}{r_1 + r_2 + \delta}. \quad (3.11)$$

Equation (3.11) is computed numerically using r_c as defined by (3.10) above.

3.4 Conductivity summary

For a model that considers conduction over a distance, as well as contact conduction we can combine equations (3.2) and (3.11) to give a piecewise

definition for G that depends on δ .

$$G(\delta) = \begin{cases} \frac{\sigma_c \pi r_c^2}{r_1 + r_2 + \delta} & \text{if } \delta < 0 \\ G_0 e^{-\gamma \delta} + G_1 & \text{if } \delta \geq 0. \end{cases} \quad (3.12)$$

Figure 3.2 shows a combined example of the results from using (3.2) to find tunnelling conduction and solving (3.11) to find the contact conduction. This plot was generated from a set of simulations with a target mean particle radius of 65 nm and target standard deviation of 9.75 nm (actual radius distribution shown in Figure 2.5). As the gap increases beyond 15 nm (not shown) the conductance continues to decay in a log-linear fashion. As the gap approaches 0 nm, the tunnelling conduction begins to increase sharply. Once contact has been made, classical charge transport dominates quickly. A minimum contact conduction is set at G_0 . In this example, this minimum is surpassed when the overlap exceeds 0.01 nm resulting in a contact radius approaching 2.5 nm. While the relationship between gap and conductivity is relatively smooth, a small amount of noise is visible and is due to the random matching of particles of differing radius.

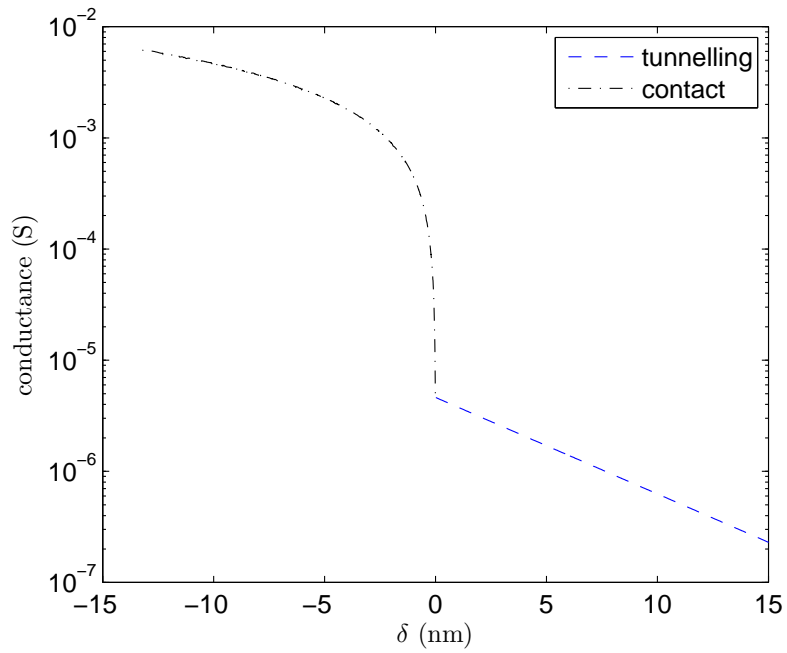


Figure 3.2: Conductance between particles arranged according to increasing gap size. Particle size varies as illustrated in Figure 2.5 and the effect of this variation can be seen as a small amount of noise in the line. A negative gap indicates particles overlap and the particles are therefore in physical contact.

Chapter 4

Results

4.1 Model size

Modelling an abundance of particles with a radius less than 100 nm in a cubic space whose edges are on the order of millimetres or larger is not computationally trivial. Models were computed on a cluster with nodes containing 8 cores and memory availability ranging from 8 to 32 GB as described in Section 2. Using this equipment to run simulations, a cubic space with edge lengths on the order of tens of microns may be simulated. It is reasonable to consider these sizes are representative of bulk conductivity provided that an edge length is chosen such that variations in edge length do not cause substantial changes in simulation results. In order to determine where that threshold lays, a series of simulations were performed with increasing edge lengths of cubic space. The time and memory required to run a simulation increases substantially with an increase in cube dimensions. For instance, to simulate a cube with an edge length of 18 μm takes about 24 hours and a cube with an edge length of 20 μm takes about 48 hours. It was found that the conductivity did not change substantially for edge lengths above 18 μm when simulating particles with a mean radius less than 100 nm at a loading of 3% by volume using the most complex modelling scenarios discussed below. This edge length value is used for all further simulations described in this work as a compromise between asymptotic saturation and model computation time. These results are shown in Figure 4.1.

4.2 Random placement of uniform particles

Uniform particles are placed randomly in 3D space as per the method described in Section 2.1.1. Particles are checked to ensure they do not overlap. Initial tests were done at 3% volume loading with particles of diameter 125 nm. The basic exponential (3.2) is used to compute conduction using G_0 as defined by (3.3).

In order to promote conduction in the model a rather low barrier height is

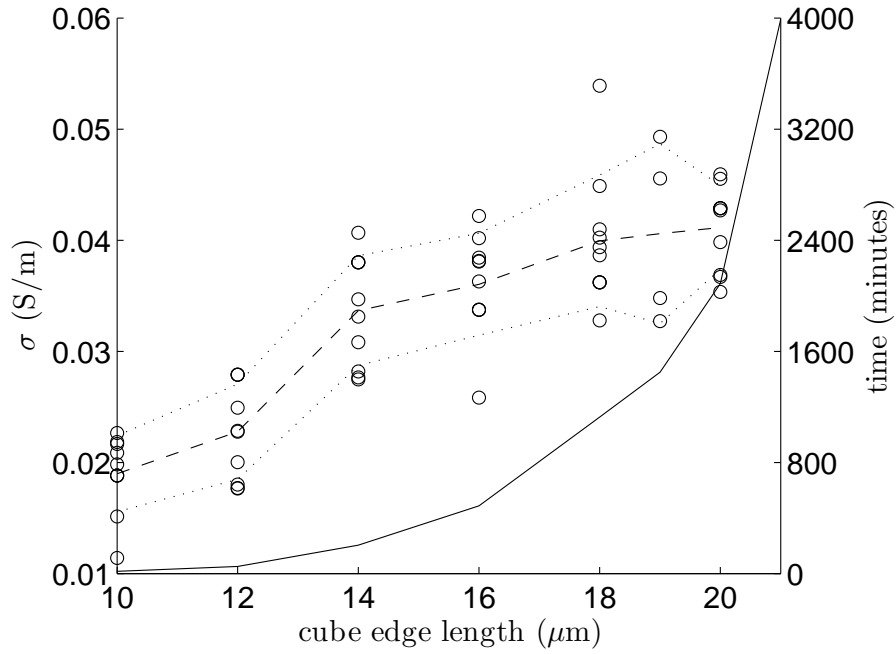


Figure 4.1: Conductivity is shown to increase asymptotically to a maximum value as the edges length of a cube being simulated increases. Individual results are shown as a circle. The long-dash line indicates mean value and the dotted lines are one standard deviation above and below the mean. The solid line shows the exponential increase in computation time as the edge size increases.

initially used, $\varphi = 0.1$ meV. This is substantially lower than barrier heights that are typical in these materials but it serves as a useful starting place as the model is developed. Using (1.4), this gives $\gamma^{-1} = 9.8$ nm. The radius of interaction is swept over a range of values to determine typical distances at which key inter-particle connections are being made. Figure 4.2 shows histogram data of connection lengths along with the associated numerical conductance per connection of that length. Figure 4.3 shows the net conductivity of the model as the radius of interaction is changed. To create this data set five simulations were run through all the steps required to place particles. Then the conductivity of each model was evaluated where the radius of interaction was swept from 100 nm to 300 nm. This effectively permits the simulation to consider, at first, only nearby neighbours, and, in the end, more distant neighbours. In each case, if the network of conductive particles does not create a complete path through the model then the resultant conductivity is that of the insulating matrix and is not shown. At a radius of interaction greater than 200 nm, all five models exhibit conductivity near $0.22 \mu\text{S/m}$. When only considering particles less than 180 nm apart, only three data points are generated; two of the models failed to exhibit end-to-end connectivity of conductive particles. With the radius of interaction below 150 nm only one of the five models continued to exhibit connectivity.

It can be concluded therefore that in order to repeatedly achieve a model with end-to-end connectivity using this particle placement method, the simulation must allow tunnelling events to occur over distances greater than 200 nm. This minimum value for the radius of interaction already uses overly optimistic potential barrier values suggesting that the placement method used fails to result in an appropriate layout of conductive particles.

4.3 Contact conduction

As described previously, the initial model calculates the tunnelling conduction between particles but as the particle generation algorithm does not permit particle edges to overlap there will not ever be a case where contact conduction occurs. By allowing a small overlap during the particle placement phase of the simulation (as described in Section 1.4), situations will arise that are analogous to the formation of agglomerates during a mixing process.

Figure 4.4 illustrates the jump in conductivity that occurs at contact. For gaps greater than zero this result is identical to that shown in Figure 4.2.

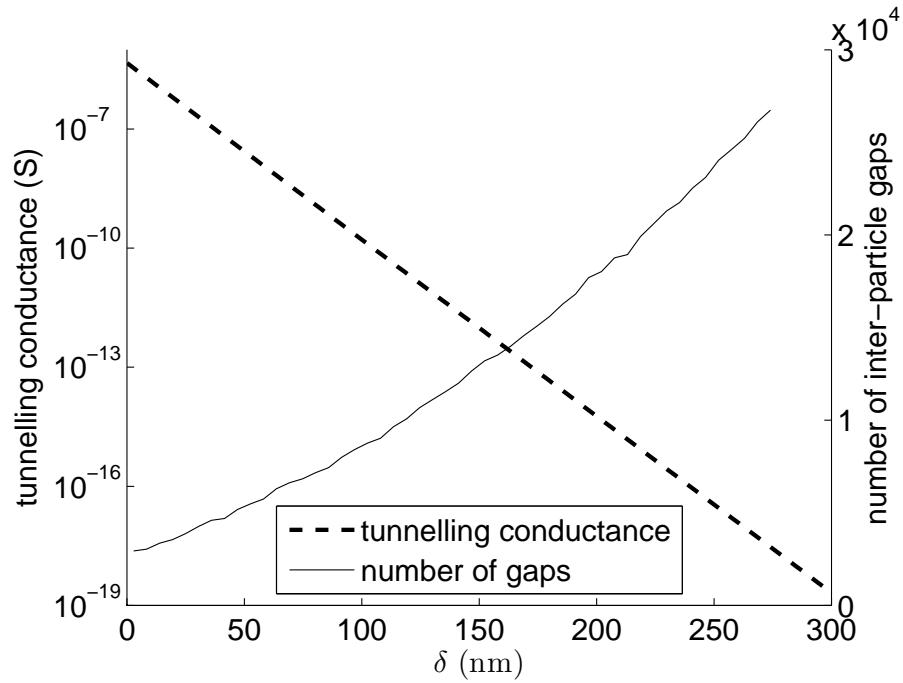


Figure 4.2: Particles that are deemed “connected” will conduct charge according to equation (3.2). The amount of conduction that occurs depends on the gap between particles. The right axis (and thin line) show histogram counts for gaps of a particular length from a typical execution of the model. Histogram bins span about 5.5 nm. For reference, the left axis (and thick dashed line) show the results of the tunnelling equation (3.2) for a gap of that size.

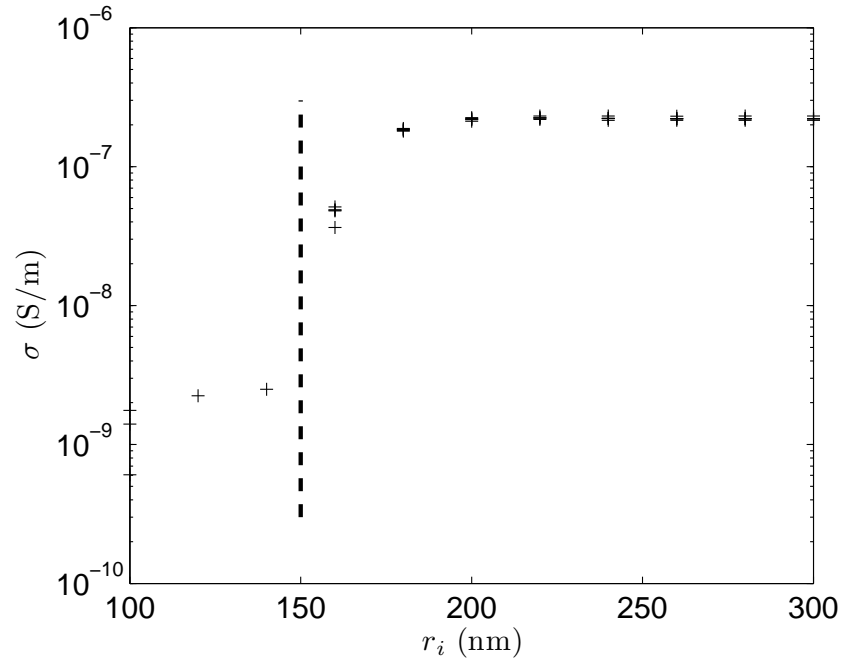


Figure 4.3: Five unique models were created with the same initial parameters (described in the text). Once each model was created, the radius of interaction was varied to create maps of connected particles. If a model exhibited end-to-end connectivity of its particles at a particular radius of interaction, a conductivity value for that combination is shown. Data to the left of the vertical dashed line is intermittent and data to the right of the vertical dashed line begins to converge.

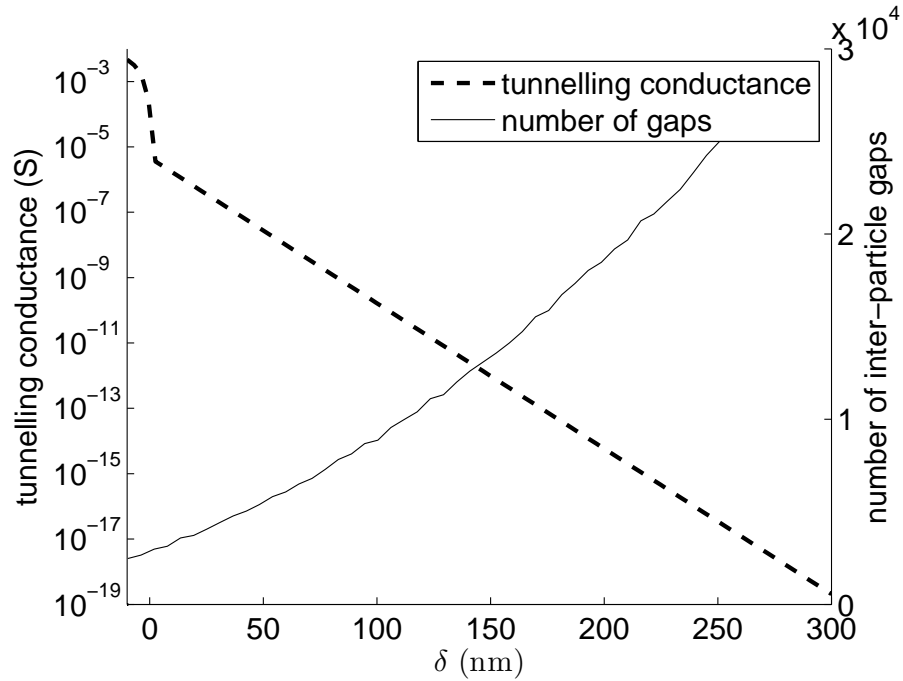


Figure 4.4: Particles with a negative inter-particle distance are said to be in contact and conduct according to equation (3.11). Particles not in physical contact that are deemed “connected” will conduct charge according to equation (3.2). The right axis (and thin line) show histogram counts for gaps of a particular length from a typical execution of the model. Histogram bins span about 5.8 nm. The left axis (and thick dashed line) show the results of the contact equation (3.11) and tunnelling equation (3.2) for a gap of that size.

As per equation (3.2), conductance between two particles is exponentially dependent on the height of the barrier between them. In Figure 4.5 results are shown for three different values of γ in order to see the effect a changing barrier height has on conductivity. Barrier heights 0.1 meV, 1 μ eV, and 10 neV are equivalent to values of γ^{-1} of 9.76 nm, 97.6 nm, and 976 nm respectively. While the units of these values and their discussion in Section 1.2 suggest a possible connection to physical properties, the values do not make sense when compared to reasonable potential barriers and reasonable tunnelling distances. To the right of the dashed vertical line, conductivities are seen to converge on a conductivity near 0.1935 μ S/m, 0.887 S/m, and 4.45 S/m respectively. It is noteworthy that although the net conductivity rises dramatically with an increasing γ^{-1} due to its place in the exponent of equation (3.2), the inter-particle distance at which the model begins to conduct remains relatively constant.

This set of results illustrates that although a model seeking to represent some of the physical realities of agglomerate formation must allow particles to physically connect in some way, the simple introduction of an algorithm to this effect has not solved problems previously described with respect to particle proximity and unrealistic tunnelling distances. The varying of γ showed an increase in the converged conductivity but did not alter the radius of interaction at which convergence began. The simulation still requires a radius of interaction above 200 nm to reliably produce results.

4.4 Clustering and filaments

In order to approximate the natural formation of filaments during the mixing and curing process an algorithm is used whereby, with a specified probability, particles must be within a specified range of a particle that has already been placed (as described in Section 2.1.3). This results in localised variability in volume loading although the bulk volume loading remains constant. As expected, specifying relatively large distances in the enforcement algorithm has no effect. Specifying progressively smaller enforced distances increases the likelihood of particles being within a short radius of interaction of each other. Specifying relatively small distances in the enforcement algorithm has the effect of many particles being within range of each other but has the side-effect of creating particle clusters that do not always connect to other clusters. To aid in the visualization of the problems described, two dimensional examples of them are shown in Figure 4.6 and Figure 4.7. Figure 4.6 shows a set of particles where the enforced proximity value is relatively large.

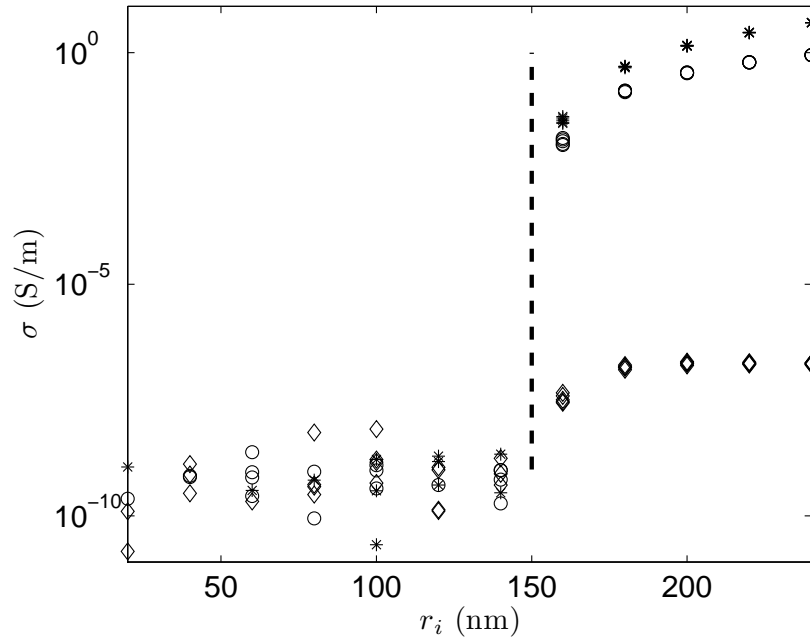


Figure 4.5: Five unique models were created with nearly all the same initial parameters to generate each set of results (each set is shown with a different symbol). The only difference between each set of model parameters is the numerical value for γ (indirectly defined by setting the barrier height to three different values). For \diamond , $\varphi = 0.1$ meV. For \circ , $\varphi = 1$ μ eV. For $*$, $\varphi = 10$ neV. Once each model was created, the radius of interaction was varied to create maps of connected particles. If a model exhibited end-to-end connectivity of its particles at a particular radius of interaction, a conductivity value for that combination is shown. Data to the left of the vertical dashed line is noisy and intermittent and data to the right of the vertical dashed line begins to converge.

It is functionally equivalent to a completely random placement and no improvements are noted. Some particles connect but rarely are more than four or five particles connected in succession. Figure 4.7 shows a set of the same number of particles where a relatively short enforced proximity has resulted in localised accumulations of particles. Where connections occur there is often a large number of particles interconnected but the structures might be better described as globs than filaments. Each of these challenges is more pronounced when considering the problem in three dimensions.

Although the enforced proximity did not immediately increase end-to-end connectivity further study was performed by sweeping through a variety of enforcement probabilities and enforcement proximities. The radius of interaction required for bulk conductivity to occur is actually larger than without the enforced proximity (an increase to about 200 nm from the 150 nm shown in Figure 4.5). The effect of this on the bulk conductivity seems apparent in Figure 4.8 where an enforced proximity of 25 nm produces a progressively lower mean conductivity as enforcement probability is increased at the upper radii of interaction. While this trend does seem to appear, overall conduction is weak and near the lower computational limits of the simulator (as described in Section 2) limiting the reliability of conclusions drawn from this data set. An optimum enforced maximum range value was found near 100 nm. This maximum range value resulted in increased formation of filaments that span the entire bulk. These results are shown in Figure 4.9. In both figures the probability of proximity enforcement is swept from 0.50 to 0.95. The effect of increased enforcement probability is shown to amplify the effects discussed above; for short range enforcement (25 nm) the bulk conductivity drops and for medium range enforcement (100 nm) the conductivity increases.

Ultimately this methodology resulted in zones of relatively higher particle density rather than forming filaments. When the higher density zones overlapped increased conductivity was observed and large portions of the model space were left without any meaningful number of conductive particles. The intention of this modelling approach was to more closely approximate experimentally observed particle distributions, including filament formation, and, as a result, exhibit better conductivity with a shorter radius of interaction. Although a set of parameters was found that improved performance at a shorter radius of interaction, the placement algorithm did not generate filament-like formations. In addition, it is difficult to reasonably defend the choice of modelling parameters used to create the optimized result.

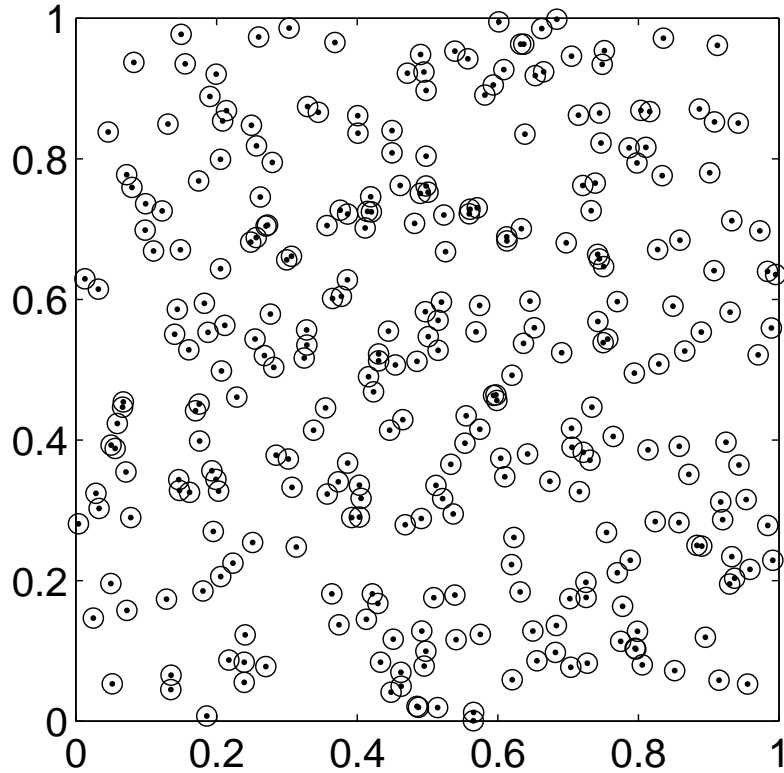


Figure 4.6: Three hundred particles are distributed in two dimensional space (arbitrary units). Seventy five of them are placed randomly and the remainder are placed in succession where each must be within 0.5 units of a previously placed particle. Each particle is shown as \cdot and its radius of interaction is shown as \circ ($r_i \approx 0.015$ units). For the purposes of this illustration, consider particles connected if their \circ 's touch. The result is similar to a random distribution. Some connections exist but rarely involving many particles.

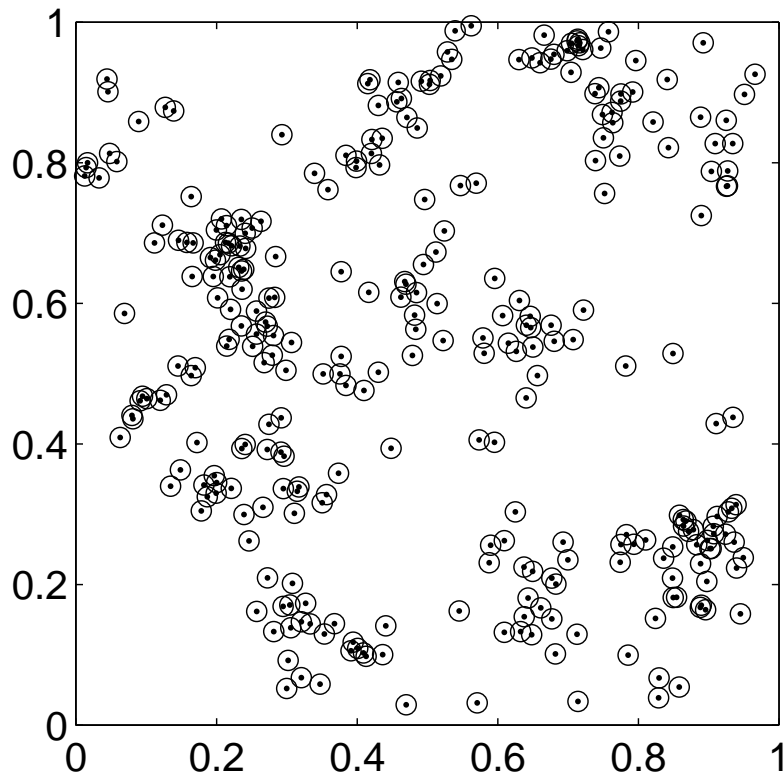


Figure 4.7: Three hundred particles are distributed in two dimensional space (arbitrary units). Seventy five of them are placed randomly and the remainder are placed in succession where each must be within 0.05 units of a previously placed particle. Each particle is shown as \cdot and its radius of interaction is shown as \circ ($r_i \approx 0.015$ units). For the purposes of this illustration, consider particles connected if their \circ 's touch. Several groupings of many particles are apparent but the groupings do not often interconnect.

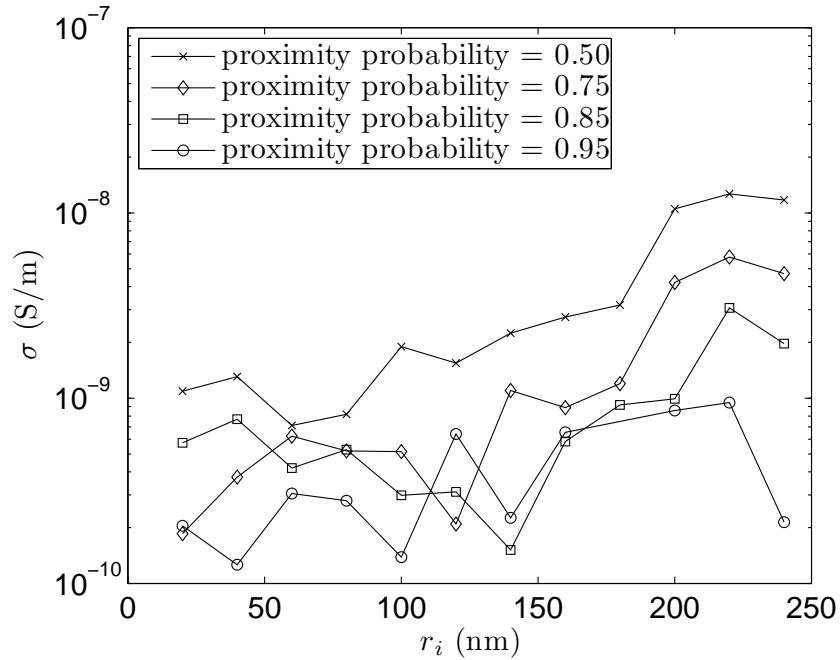


Figure 4.8: Conductivity values as a function of radius of interaction when an enforced proximity of 25 nm is implemented. Each data point represents the mean result of five simulations and each line is associated with a different enforcement probability as shown in the legend. Overall volume loading of particles is held constant at $\phi = 0.03$. As described in Section 2, conductivities near 10^{-9} S/m are of unreliable precision due to a near-singularity during matrix inversion. This accounts for the erratic low mean conductivity values.

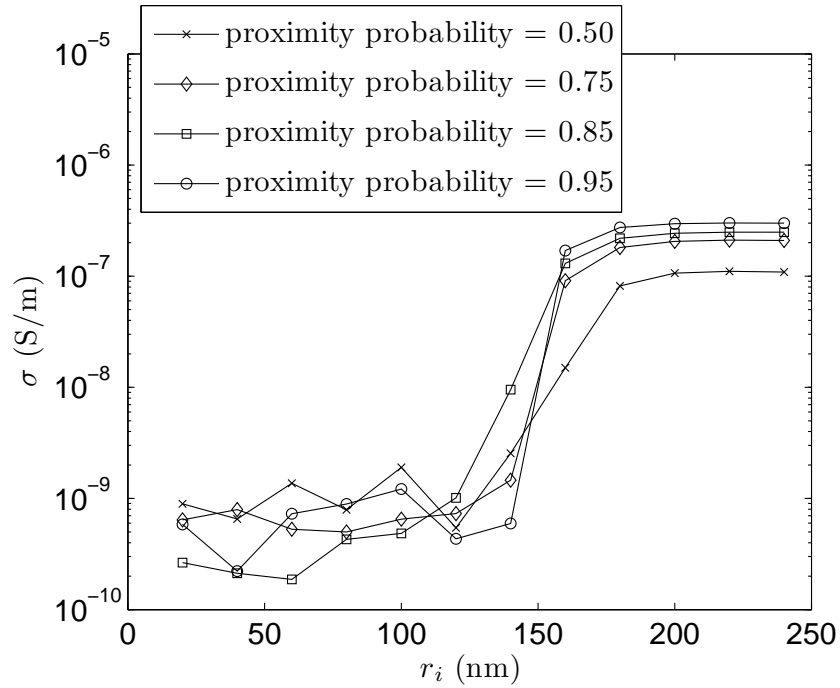


Figure 4.9: Conductivity values as a function of radius of interaction when an enforced proximity of 100 nm is implemented. Each data point represents the mean result of five simulations and each line is associated with a different enforcement probability as shown in the legend. Overall volume loading of particles is held constant at $\phi = 0.03$.

4.5 Voronoi cell network

Implementing a node networking scheme that more closely follows a Voronoi network as described in Section 2.1.4 resulted in a substantial jump in model conductivity. Key model parameters are the quantity of Voronoi cells occurring per unit volume, v_{dens} , and the maximum thickness of the filaments formed, v_{rMax} . Values for v_{dens} were determined empirically by running successive simulations and comparing the resultant cell edge lengths to typical values as described in Section 2.1.4. Cell edge lengths were targeted to be in the range from several nm's to 10's μm . This was found to occur in models with $10^6 \text{ mm}^{-3} < v_{dens} < 10^7 \text{ mm}^{-3}$. Figure 4.10 shows an example histogram of edge lengths for a model with a target density of $v_{dens} = 5 \times 10^6 \text{ mm}^{-3}$.

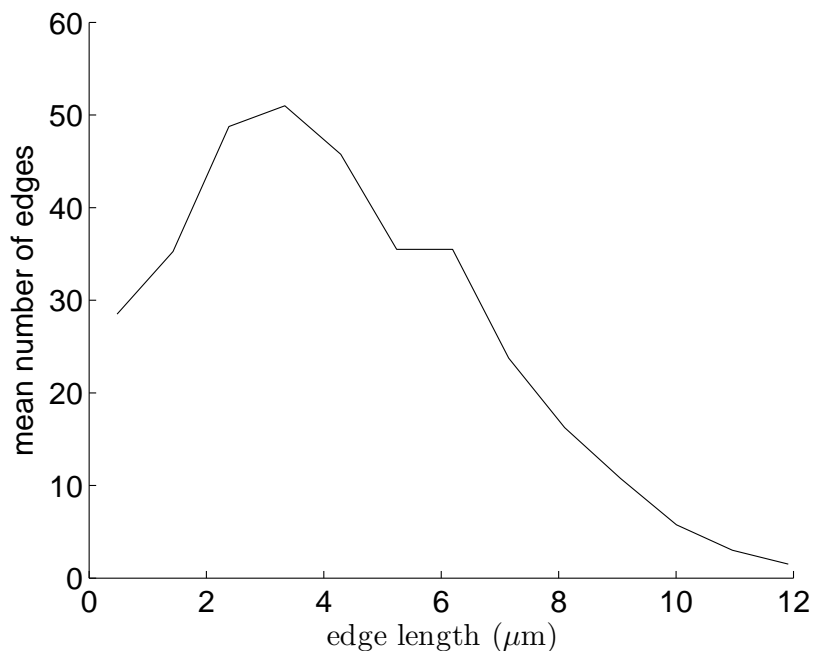


Figure 4.10: Histogram data of typical mean edge lengths for a model with a target density of $v_{dens} = 5 \times 10^6 \text{ mm}^{-3}$. Each histogram bin spans about $0.95 \mu\text{m}$.

Filament maximum thickness values were swept from 10 to 30 times the mean particle radius. In this case that equates to approximately $1 \mu\text{m}$

$< v_{rMax} < 2 \mu\text{m}$. The de-facto minimum thickness is the diameter one particle (or possibly no particles as the case may be). This range of model inputs is consistent with the works described in Section 1.3. The filaments are not forced to be consistently of the thickness defined by v_{rMax} , rather they are permitted to contain bulges and narrows provided none of the bulges exceed the defined maximum thickness. Figure 4.11 shows the results of this v_{rMax} sweep as a function of volume loading and gives the resultant model conductivity. Each parameter set shows a conductivity evolution with a similar trend as loading increases. The thicker filaments likely exhibit slightly lower conductivity because they result in conductive particles spread more radially along the axis of the filament whereas a narrower filament restricts the particles to more confined and regular filaments. For reference, Figure 4.12 shows the results of the $v_{rMax} = 1.06 \mu\text{m}$ sweep within the context of the experimental results previously shown and individually attributed in Figure 1.8. Also shown for reference are converged values from results previously discussed and shown in Figures 4.3, 4.5, and 4.9. The Voronoi model produces a trend line that runs parallel to those measured in experiments with carbon black and polydimethylsiloxane. Despite the shape of the results being similar, it is apparent that the magnitude of the Voronoi model data (about 10^{-3} S/m at 3% volume loading) is substantially smaller than the magnitude of the experimental data (about 10^{-1} S/m at 3% volume loading). The previously used modelling methods all generated results even smaller (about 10^{-6} S/m at 3% volume loading). Also included for reference is an upper limit to carbon conductivity. The limit is computed by considering all carbon matter present at a particular volume loading arranged into a column that perfectly and uniformly connects through the model space.

The Voronoi model data takes on a shape that conforms to the power law behaviour discussed in Section 1.1. Figure 4.13 compares that data to equation(1.2) with $\phi_c = 0.05$ and $t = 5$. A constant of proportionality, 10^5 , is applied to overlap the power law shape with the model data. When performing the fit an appropriate value for ϕ_c is not immediately clear. It represents the inflection point of the power law curve. In the case of these model results that point is below the minimum computable conductivity. The parameters chosen give a reasonable fit across the data available. Balberg’s assertions suggest this value of t indicates the particles are “more spherical” though more quantitative implications remain unclear [17].

In order to ensure end-to-end model connectivity during model development, the radius of interaction has been maintained relatively high such that conduction decay is dependant on the value of φ . The latest models were repeated while evaluating the variation in conductivity as a function

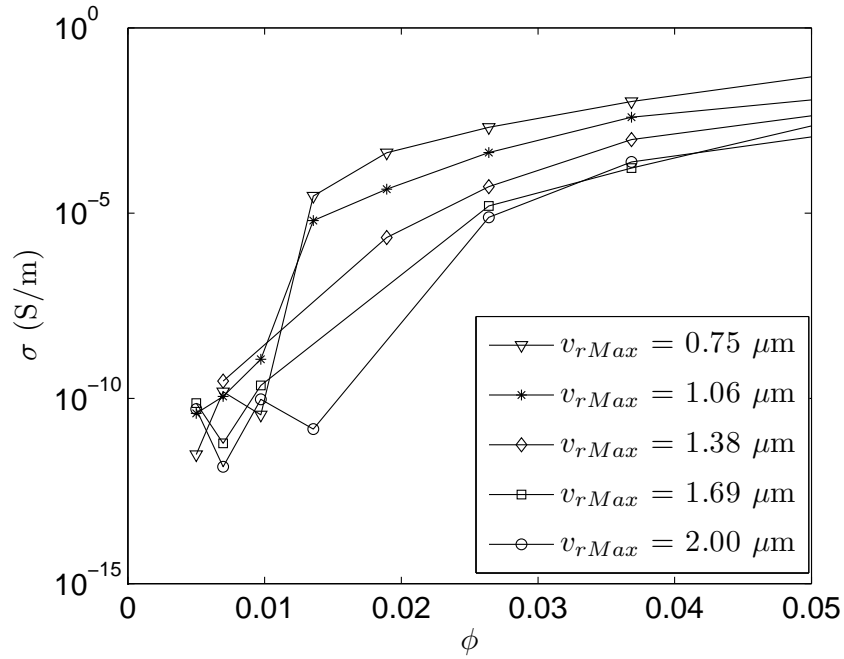


Figure 4.11: Conductivity as a function of volume loading for a range of filament radius values.

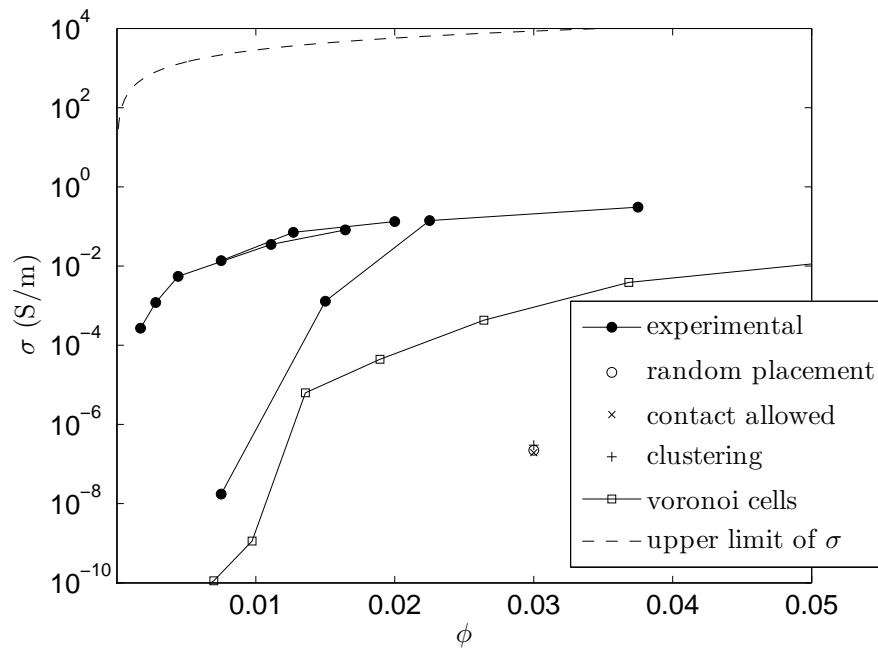


Figure 4.12: Model results are shown here with published experimental data [8, 9]. (Individual attributions are shown in Figure 1.8.) Model results are those previously shown in Figures 4.3, 4.5, 4.9, and 4.11. For reference, the upper limit of conductivity is also shown.

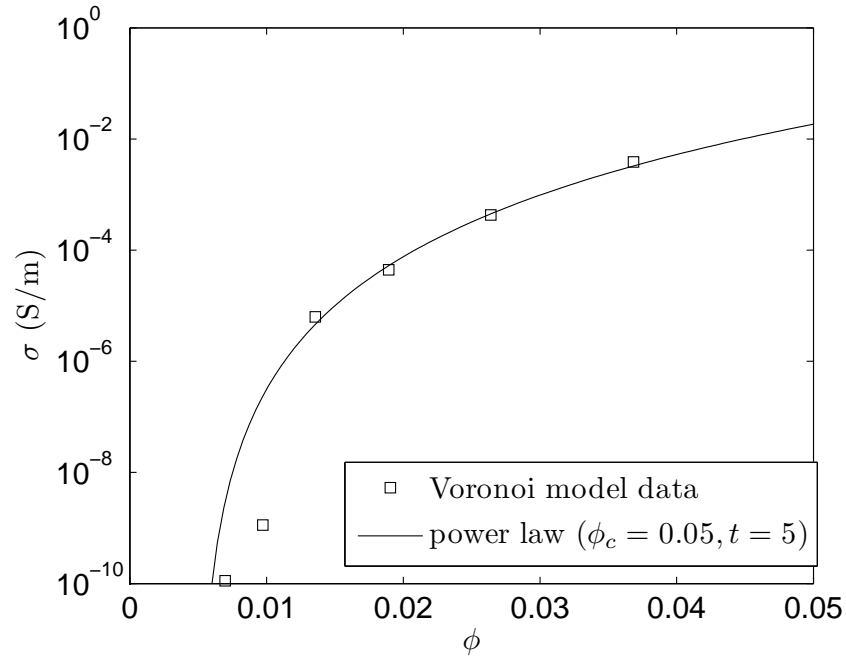


Figure 4.13: Voronoi model results are compared to a line fit for the power law behaviour discussed in Section 1.1.

of radius of interaction. This is illustrated in Figure 4.14 for four different volume loadings.

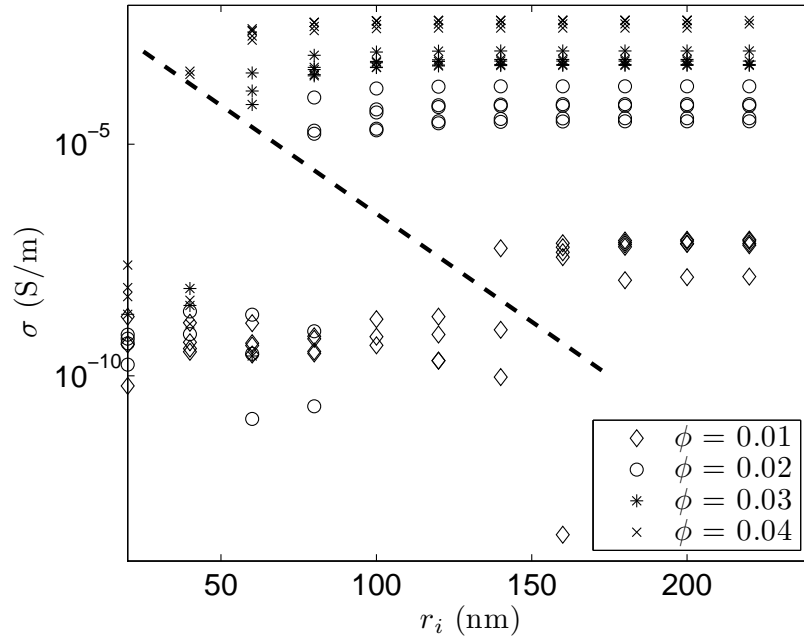


Figure 4.14: Conductivity as a function of radius of interaction for four different volume loadings. Data to the lower-left of the dashed line is noisy and intermittent in end-to-end connectivity and data to the upper-right of the dashed line is convergent.

In contrast to prior plots of conductivity vs radius of interaction, in Figure 4.14 it is clear that end-to-end connectivity occurs when considering neighbours less than 100 nm apart, an improvement over prior iterations of the model. The saturation of conductivity that occurs shortly after connectivity first occurs is illustrative of the exponential dependence on distance in tunnelling scenarios. This overall improvement is attributed to the filaments represented by the Voronoi network. Although the minimum radius of interaction needed for each of the simulation sets shown in Figure 4.14 is greater than might be expected for a tunnelling scenario, it is an improvement over prior models.

Chapter 5

Conclusions and future work

5.1 Conclusions

The model created and evaluated as part of this work synthesizes theory drawn from first principles, theoretical explanations of observed phenomena, and basic analysis of experimental data. The semi-empirical approach used combines many parameters, most of which can be said to have a physical interpretation. Many previous works have neglected these physical interpretations in favour of good agreement between analytical expressions and the data being published concurrently with those expressions. This model differentiates itself by identifying obvious or potential physical meaning behind constants that could otherwise be treated as simple fitting parameters. In cases where parameters are permitted to move outside apparently reasonable bounds a discussion of assumptions and motivations is provided.

A great deal of uncertainty can be found in the parameter γ and, through the relationship defined in (1.4), φ in the tunnelling conduction exponential. Although the physics describing the height of the barrier being tunnelled through holds in simple situations such as with a scanning tunnelling microscope, it seems apparent that in the case of many conductive composites there are more factors that warrant consideration. While not clearly understood they either modify or act in addition to barrier height effects. Rather than introduce additional parameters, these effects are left bundled in the barrier height parameter to illustrate this gap in understanding.

The initial model shows that a random distribution of spherical particles, given realistic γ and φ , cannot explain experimentally observed conductivities in these composite materials. The final model shows conductivity in simulations loaded less than $\phi = 5\%$ by volume. The conductivity is several orders of magnitude lower than experimental results that use carbon particles of similar dimension and upon whose structure the model was based. This discrepancy further illustrates that the model still lacks a comprehensive set of physics and input parameters.

Ultimately, it shows that bulk conductivity at loadings well below the classical percolation threshold can be simulated by combining known physics

with empirical observations of micro-structure in conductive composites created using particles on the size order of 200 nm and smaller. The trend in simulation results agrees with the trends observed in published experimental data. The differences between the simulation results and the experimental results serve to motivate future exploration of these materials in pursuit of a more complete understanding of the phenomena at work.

5.2 MATLAB as a modelling tool

All simulations were conducted in MATLAB Version 7.9.0.529 (R2009b). Most algorithms were tested on a standard laptop computer before execution on the high performance computing cluster described in Section 2. Compute time for simulations was a key concern during model development. The core algorithm for serially generating lists of locations in space for particle placement and the earliest version of the user interface were created by Liam Russel in 2010. A serial approach to subsequent modelling algorithms followed naturally from this start. As model complexity grew the compute time for modelling also grew rapidly, in part due to its serial nature. Most model components were later rewritten to take advantage of memory allocation and parallel processing functionality in MATLAB. A model that was designed with the intention of performing parallel operations at all possible times could serve to improve simulation durations on a platform such as a high performance computing cluster.

Long compute times (during development they reached over seven days for a single simulation), although undesirable, can be overcome with patience. The most substantial obstacle to model computation was the cubic growth in memory requirements as the model size increased with one particular matrix inversion making the greatest draw on resources. On several occasions memory usage exceeded the capability of the computing cluster and resulted in a failure of the simulation after many hours or days of computation.

MATLAB provides a good set of tools for developing parallel processing algorithms and for memory management. Ultimately the limitations described above can be attributed somewhat to choice of modelling algorithms and predominantly to hardware limitations.

5.3 Future work

5.3.1 Greater complexity in modelling parameters

One approach to increasing the “realism” of this model would be to incorporate more first principles physics and more empirical observations. For instance, incorporating a set of modelling routines that move particles according to physical processes at work during mixing could offer additional insight. This approach could take advantage of known surface tension effects that affect agglomeration and filament formation. The model could also be modified to incorporate the assertion by Kohijiya that aggregates closer than 3 nm tend to fuse into agglomerates and that freshly broken agglomerates tend to separate by 3 nm [5].

A series of experiments could be done to determine whether hopping or tunnelling is dominant. The processes could be differentiated by observing the temperature variance of conduction. The temperature dependence of hopping may reveal whether or not this phenomenon warrants inclusion in models of this sort.

One caution though is that the incorporation of any poorly understood parameters can lead to greater uncertainty in the model and may ultimately over-tune it in the same way that adding additional high order components to a line fit may seem at first to give better results even if it is not really revealing more about the governing mechanisms.

5.3.2 Post-curing analysis of carbon black

Further analysis of the size and shape of carbon aggregates and agglomerates that have undergone a mixing and curing process is warranted.

Despite difficulties slicing thin samples of many conductive composite materials, it is ultimately possible to cool a sample sufficiently for thin slices to be made. Combining a cryostat microtome with high resolution imaging tools could shed substantial light on the structures formed by carbon black in the scenarios being considered by this model. A challenge in doing this is that many cryotomes have a lowest operating temperature near $-40\text{ }^{\circ}\text{C}$ as they are designed for biological systems. In those systems softer rubbers such polydimethylsiloxane may not be sufficiently frozen to produce a clean cut. Once that obstacle is overcome and the corresponding digital images are analysed, the resultant numerical data describing a range of micro or nano scale physical parameters for a suite of composites could prove instrumental in the further tuning of this model or the creation of a new one.

To gain further insight into the carbon black it may be valuable to gently dissolve the polymer component of a cured sample and then image the precipitated carbon particles with as little disturbance as possible. A comparison with imaging and size profiling of the same carbon done pre-curing may prove insightful.

5.3.3 Alternate techniques

At the outset it was hoped this model could be used as a predictive tool to anticipate the electrical characteristics of conductive composites and that it could then be further refined to explore the importance of deformation of irregular geometries in future applications. The approach taken was one that captured and described the inter-particle charge transport phenomenon at work within the composite. As a result of this choice it does offer insight into those physics but it falls short of being a true predictive model. While a truly predictive model that relies solely on governing physics may be the most satisfying solution, the present gaps in understanding suggest there is work to be done before that model exists. In the interim it may be useful to divide the approach in two. The present model can be expanded and refined to become a better representation of the science behind conductive composites while a separate model may be useful as a purely predictive tool. The purely predictive tool could potentially take more of a “black-box” approach that did not consider physics but rather simply considered input and output parameters and is trained against known data using the wide range of adaptive machine learning algorithms available in the field of computer science.

Bibliography

- [1] X.-W. Zhang, Y. Pan, Q. Zheng, and X.-S. Yi, “Time dependence of piezoresistance for the conductor-filled polymer composites,” *Journal of Polymer Science Part B: Polymer Physics*, vol. 38, pp. 2739–2749, Nov. 2000.
- [2] S. Wang, P. Wang, and T. Ding, “Resistive viscoelasticity of silicone rubber/carbon black composite,” *Polymer Composites*, vol. 32, pp. 29–35, Jan. 2011.
- [3] J. Meier, J. Mani, and M. Klüppel, “Analysis of carbon black network-ing in elastomers by dielectric spectroscopy,” *Physical Review B*, vol. 75, p. 054202, Feb. 2007.
- [4] D. M. Heyes, M. Cass, and A. C. Branka, “Percolation threshold of hard-sphere fluids in between the soft-core and hard-core limits,” *Molec-ular Physics*, vol. 104, pp. 3137–3146, Oct. 2006.
- [5] S. Kohjiya, A. Kato, and Y. Ikeda, “Visualization of nanostructure of soft matter by 3D-TEM: Nanoparticles in a natural rubber matrix,” *Progress in Polymer Science*, vol. 33, pp. 979–997, Oct. 2008.
- [6] J. Bang, K. Han, S. Skrabalak, H. Kim, and K. Suslick, “Porous Carbon Supports Prepared by Ultrasonic Spray Pyrolysis for Direct Methanol Fuel Cell Electrodes,” *Journal of Physical Chemistry C*, vol. 111, pp. 10959–10964, July 2007.
- [7] X. Z. Niu, S. L. Peng, L. Y. Liu, W. J. Wen, and P. Sheng, “Char-acterizing and Patterning of PDMS-Based Conducting Composites,” *Advanced Materials*, vol. 19, pp. 2682–2686, Sept. 2007.
- [8] R. S.-P., K. F.-H., and C. K.-C., “Dispersion of carbon black in a continuous phase: Electrical, rheological, and morphological studies,” *Colloid & Polymer Science*, vol. 280, pp. 1110–1115, Dec. 2002.
- [9] A. Linklater, “Characterisation of Vulcan XC72 in PDMS composites,” *UBC Internal report*, 2012.

- [10] Z. H. Li, “Effects of carbon blacks with various structures on vulcanization and reinforcement of filled ethylene-propylene-diene rubber,” *eXPRESS Polymer Letters*, vol. 2, pp. 695–704, Sept. 2008.
- [11] J.-C. Huang, “Carbon black filled conducting polymers and polymer blends,” *Advances in Polymer Technology*, vol. 21, pp. 299–313, Jan. 2002.
- [12] J.-C. Huang and C.-L. Wu, “Processability, mechanical properties, and electrical conductivities of carbon black-filled ethylene-vinyl acetate copolymers,” *Advances in Polymer Technology*, vol. 19, pp. 132–139, Jan. 2000.
- [13] Z. Y. Liu, J. L. Zhang, P. T. Yu, J. X. Zhang, R. Makharia, K. L. More, and E. a. Stach, “Transmission Electron Microscopy Observation of Corrosion Behaviors of Platinized Carbon Blacks under Thermal and Electrochemical Conditions,” *Journal of The Electrochemical Society*, vol. 157, no. 6, p. B906, 2010.
- [14] J. Strumpler, R. and Glatz-Reichenbach, “Conducting Polymer Composites,” *Journal of Electroceramics*, vol. 3, no. 4, pp. 329–346, 1999.
- [15] M. Knite, V. Teteris, A. Kiploka, and J. Kaupuzs, “Polyisoprene-carbon black nanocomposites as tensile strain and pressure sensor materials,” *Sensors and Actuators A: Physical*, vol. 110, pp. 142–149, Feb. 2004.
- [16] G. Ambrosetti, C. Grimaldi, I. Balberg, T. Maeder, A. Danani, and P. Ryser, “Solution of the tunneling-percolation problem in the nanocomposite regime,” *Physical Review B*, vol. 81, p. 155434, Apr. 2010.
- [17] I. Balberg, “A comprehensive picture of the electrical phenomena in carbon blackpolymer composites,” *Carbon*, vol. 40, pp. 139–143, Feb. 2002.
- [18] J. Kubát, R. Kužel, I. Kivka, P. Bengtsson, J. Prokeš, and O. Stefan, “New conductive polymeric systems,” *Synthetic Metals*, vol. 54, pp. 187–194, Mar. 1993.
- [19] I. Balberg, “Tunneling and nonuniversal conductivity in composite materials,” *Physical Review Letters*, vol. 59, pp. 1305–1308, Sept. 1987.

- [20] R. Newnham, D. Skinner, and L. Cross, "Connectivity and piezoelectric-pyroelectric composites," *Materials Research Bulletin*, vol. 13, pp. 525–536, May 1978.
- [21] S. Kirkpatrick, "Percolation and Conduction," *Reviews of Modern Physics*, vol. 45, pp. 574–588, Oct. 1973.
- [22] W. Y. Hsu, W. G. Holtje, and J. R. Barkley, "Percolation phenomena in polymer/carbon composites," *Journal of Materials Science Letters*, vol. 7, pp. 459–462, May 1988.
- [23] S. Vionnet-Menot, C. Grimaldi, T. Maeder, S. Strässler, and P. Ryser, "Tunneling-percolation origin of nonuniversality: Theory and experiments," *Physical Review B*, vol. 71, p. 064201, Feb. 2005.
- [24] W. Bauhofer and J. Z. Kovacs, "A review and analysis of electrical percolation in carbon nanotube polymer composites," *Composites Science and Technology*, vol. 69, pp. 1486–1498, Aug. 2009.
- [25] W. Zhang, A. a. Dehghani-Sani, and R. S. Blackburn, "Carbon based conductive polymer composites," *Journal of Materials Science*, vol. 42, pp. 3408–3418, Mar. 2007.
- [26] X. Zhang, Y. Pan, Q. Zheng, and X. Yi, "Piezoresistance of conductor filled insulator composites," *Polymer International*, vol. 50, pp. 229–236, Feb. 2001.
- [27] J. G. Simmons, "Low-Voltage Current-Voltage Relationship of Tunnel Junctions," *Journal of Applied Physics*, vol. 34, no. 1, p. 238, 1963.
- [28] J. G. Simmons, "Electric Tunnel Effect between Dissimilar Electrodes Separated by a Thin Insulating Film," *Journal of Applied Physics*, vol. 34, no. 9, p. 2581, 1963.
- [29] J. G. Simmons, "Generalized Formula for the Electric Tunnel Effect between Similar Electrodes Separated by a Thin Insulating Film," *Journal of Applied Physics*, vol. 34, no. 6, p. 1793, 1963.
- [30] J. G. Simmons and G. J. Unterkofer, "Potential Barrier Shape Determination in Tunnel Junctions," *Journal of Applied Physics*, vol. 34, no. 6, p. 1828, 1963.
- [31] P. Bagwell and T. Orlando, "Landauers conductance formula and its generalization to finite voltages," *Physical Review B*, vol. 40, pp. 1456–1464, July 1989.

- [32] F. Bassani, G. L. Liedl, P. Wyder, J. Gomez-Herrero, and R. Reifemberger, "Scanning Probe Microscopy," *Encyclopedia of Condensed Matter Physics*, pp. 172–182, 2005.
- [33] P. K. Hansma and J. Tersoff, "Scanning tunneling microscopy," *Journal of Applied Physics*, vol. 61, no. 2, p. R1, 1987.
- [34] C. J. Chen, *Introduction to Scanning Tunneling Microscopy*. Oxford University Press, 2 ed., 2008.
- [35] D. Bloor, K. Donnelly, P. J. Hands, P. Laughlin, and D. Lussey, "A metalpolymer composite with unusual properties," *Journal of Physics D: Applied Physics*, vol. 38, pp. 2851–2860, Aug. 2005.
- [36] G. Ambrosetti, N. Johner, C. Grimaldi, T. Maeder, P. Ryser, and A. Danani, "Electron tunneling in conductor-insulator composites with spherical fillers," *Journal of Applied Physics*, vol. 106, no. 1, p. 016103, 2009.
- [37] S. Kato, K. Hashimoto, and K. Watanabe, "Microbial interspecies electron transfer via electric currents through conductive minerals.," *Proceedings of the National Academy of Sciences of the United States of America*, vol. 109, pp. 10042–6, June 2012.
- [38] L. E. Levine, G. G. Long, J. Ilavsky, R. a. Gerhardt, R. Ou, and C. a. Parker, "Self-assembly of carbon black into nanowires that form a conductive three dimensional micronetwork," *Applied Physics Letters*, vol. 90, no. 1, p. 014101, 2007.
- [39] H.-P. Xu, Z.-M. Dang, D.-H. Shi, and J.-B. Bai, "Remarkable selective localization of modified nanoscaled carbon black and positive temperature coefficient effect in binary-polymer matrix composites," *Journal of Materials Chemistry*, vol. 18, no. 23, p. 2685, 2008.
- [40] J. Fröhlich, W. Niedermeier, and H.-D. Luginsland, "The effect of filler-filler and fillere elastomer interaction on rubber reinforcement," *Composites Part A: Applied Science and Manufacturing*, vol. 36, pp. 449–460, Apr. 2005.
- [41] O. A. Al-Hartomy, F. Al-Solamy, A. Al-Ghamdi, N. Dishovsky, M. Ivanov, M. Mihaylov, and F. El-Tantawy, "Influence of Carbon Black Structure and Specific Surface Area on the Mechanical and Dielectric Properties of Filled Rubber Composites," *International Journal of Polymer Science*, vol. 2011, pp. 1–8, 2011.

- [42] T. Koga, T. Hashimoto, M. Takenaka, K. Aizawa, N. Amino, M. Nakamura, D. Yamaguchi, and S. Koizumi, "New Insight into Hierarchical Structures of Carbon Black Dispersed in Polymer Matrices: A Combined Small-Angle Scattering Study," *Macromolecules*, vol. 41, pp. 453–464, Jan. 2008.
- [43] T. Koga, M. Takenaka, K. Aizawa, M. Nakamura, and T. Hashimoto, "Structure factors of dispersible units of carbon black filler in rubbers.," *Langmuir : the ACS journal of surfaces and colloids*, vol. 21, pp. 11409–13, Nov. 2005.
- [44] S. Kohjiya, A. Katoh, T. Suda, J. Shimanuki, and Y. Ikeda, "Visualisation of carbon black networks in rubbery matrix by skeletonisation of 3D-TEM image," *Polymer*, vol. 47, pp. 3298–3301, May 2006.
- [45] N. Kchit and G. Bossis, "Electrical resistivity mechanism in magnetorheological elastomer," *Journal of Physics D: Applied Physics*, vol. 42, p. 105505, May 2009.
- [46] W. F. Verhelst, K. G. Wolthuis, A. Voet, P. Ehrburger, and J. B. Donnet, "The Role of Morphology and Structure of Carbon Blacks in the Electrical Conductance of Vulcanizates," *Rubber Chemistry and Technology*, vol. 50, pp. 735–746, Sept. 1977.
- [47] T. Brown, H. Lemay, and B. Bursten, *Chemistry: The Central Science*. Simon & Schuster, 1997.
- [48] Cabot Corporation, "Vulcan XC72 Data Sheet," 2004.
- [49] C. W. Lee, "Effect of Binary Conductive Agents in Spinel LiMn₂O₄ Cathodes on Electrochemical Performance of Li-ion Batteries," *Journal of industrial and engineering chemistry*, vol. 12, no. 6, pp. 967–971, 2006.
- [50] A. Clague, J. Donnet, T. Wang, and J. Peng, "A comparison of diesel engine soot with carbon black," *Carbon*, vol. 37, pp. 1553–1565, Jan. 1999.
- [51] A. Kato, J. Shimanuki, S. Kohjiya, and Y. Ikeda, "Three-Dimensional Morphology of Carbon Black in NR Vulcanizates as Revealed by 3D-Tem and Dielectric Measurements," *Rubber Chemistry and Technology*, vol. 79, pp. 653–673, Sept. 2006.

- [52] D. S. McLachlan, “A grain consolidation model for the critical or percolation volume fraction in conductor-insulator mixtures,” *Journal of Applied Physics*, vol. 70, no. 7, p. 3681, 1991.
- [53] D. S. McLachlan, “Analytical Functions for the dc and ac Conductivity of Conductor-Insulator Composites,” *Journal of Electroceramics*, vol. 5, no. 2, pp. 93–110, 2000.
- [54] A. Jean, D. Jeulin, S. Forest, S. Cantournet, and F. N’guyen, “A multiscale microstructure model of carbon black distribution in rubber,” *Journal of microscopy*, vol. 241, pp. 243–60, Mar. 2011.
- [55] S. Kumar and S. K. Kurtz, “Simulation of material microstructure using a 3D voronoi tessellation: Calculation of effective thermal expansion coefficient of polycrystalline materials,” *Acta Metallurgica et Materialia*, vol. 42, pp. 3917–3927, Dec. 1994.
- [56] Z. Fan, Y. Wu, X. Zhao, and Y. Lu, “Simulation of polycrystalline structure with Voronoi diagram in Laguerre geometry based on random closed packing of spheres,” *Computational Materials Science*, vol. 29, pp. 301–308, Mar. 2004.
- [57] D. F. Watson, “Computing the n-dimensional Delaunay tessellation with application to Voronoi polytopes,” *The Computer Journal*, vol. 24, pp. 167–172, Feb. 1981.
- [58] P. Dong, “Generating and updating multiplicatively weighted Voronoi diagrams for point, line and polygon features in GIS,” *Computers & Geosciences*, vol. 34, pp. 411–421, Apr. 2008.
- [59] G. Ambrosetti, N. Johner, C. Grimaldi, A. Danani, and P. Ryser, “Percolative properties of hard oblate ellipsoids of revolution with a soft shell,” *Physical Review E*, vol. 78, p. 061126, Dec. 2008.
- [60] I. Balberg and N. Binenbaum, “Invariant properties of the percolation thresholds in the soft-core/hard-core transition,” *Physical Review A*, vol. 35, pp. 5174–5177, June 1987.

Appendix A

Simulation parameters

Contained herein is a list of relevant modelling parameters for figures generated using the model described throughout this document.

Parameters for Figure 2.5

$$\phi = 3\%$$

$$r = 65 \text{ nm (log normal deviation target} = 15\%)$$

$$G_0 = 4.62 \mu\text{S}$$

$$\gamma^{-1} = 9.76 \text{ nm}$$

$$\varphi = 0.1 \text{ meV}$$

$$v_{dens} = 5 \times 10^6 \text{ mm}^{-3}$$

$$v_{rMax} = 1.0625 \mu\text{m}$$

$$r_i = 100 \text{ nm}$$

Parameters for Figure 4.1

$$\phi = 3\%$$

$$r = 62.5 \text{ nm (log normal deviation target} = 10\%)$$

$$G_0 = 4.62 \mu\text{S}$$

$$\gamma^{-1} = 9.76 \text{ nm}$$

$$\varphi = 0.1 \text{ meV}$$

$$v_{dens} = 10 \times 10^6 \text{ mm}^{-3}$$

$$v_{rMax} = 187.5 \text{ nm}$$

$$r_i = 275 \text{ nm}$$

Parameters for Figure 4.2

$$\phi = 3\%$$

$$r = 62.5 \text{ nm (log normal deviation target = 10\%)}$$

$$G_0 = 4.62 \mu\text{S}$$

$$\gamma^{-1} = 9.76 \text{ nm}$$

$$\varphi = 0.1 \text{ meV}$$

Parameters for Figure 4.3

$$\phi = 3\%$$

$$r = 62.5 \text{ nm (log normal deviation target = 10\%)}$$

$$G_0 = 4.62 \mu\text{S}$$

$$\gamma^{-1} = 9.76 \text{ nm}$$

$$\varphi = 0.1 \text{ meV}$$

$$r_i = \text{varies as per x-axis}$$

Parameters for Figure 4.4

$$\phi = 3\%$$

$$r = 62.5 \text{ nm (log normal deviation target = 10\%)}$$

$$G_0 = 4.62 \mu\text{S}$$

$$\gamma^{-1} = 9.76 \text{ nm}$$

$$\varphi = 0.1 \text{ meV}$$

Parameters for Figure 4.5

$$\phi = 3\%$$

$$r = 62.5 \text{ nm (log normal deviation target = 10\%)}$$

$$G_0 = 4.62 \mu\text{S}$$

$$\gamma^{-1} = \text{varies as per figure description}$$

φ = varies as per figure description

$$v_{dens} = 10^8 \text{ mm}^{-3}$$

$$v_{rMax} = 187.5 \text{ nm}$$

r_i = varies as per x-axis

Parameters for Figure 4.8

$$\phi = 3\%$$

$r = 65 \text{ nm}$ (log normal deviation target = 15%)

$$G_0 = 4.62 \mu\text{S}$$

$$\gamma^{-1} = 9.76 \text{ nm}$$

$$\varphi = 0.1 \text{ meV}$$

r_i = varies as per x-axis

enforced proximity = 25 nm

probability of enforced proximity = varies as per legend

Parameters for Figure 4.9

$$\phi = 3\%$$

$r = 65 \text{ nm}$ (log normal deviation target = 15%)

$$G_0 = 4.62 \mu\text{S}$$

$$\gamma^{-1} = 9.76 \text{ nm}$$

$$\varphi = 0.1 \text{ meV}$$

r_i = varies as per x-axis

enforced proximity = 100 nm

probability of enforced proximity = varies as per legend

Parameters for Figure 4.10

$$\phi = 3\%$$

$$r = 65 \text{ nm (log normal deviation target = 15\%)}$$

$$G_0 = 4.62 \mu\text{S}$$

$$\gamma^{-1} = 9.76 \text{ nm}$$

$$\varphi = 0.1 \text{ meV}$$

$$v_{dens} = 5 \times 10^6 \text{ mm}^{-3}$$

$$v_{rMax} = 187.5 \text{ nm}$$

$$r_i = 100 \text{ nm}$$

Parameters for Figure 4.11

$$\phi = \text{varies as per x-axis}$$

$$r = 65 \text{ nm (log normal deviation target = 15\%)}$$

$$G_0 = 4.62 \mu\text{S}$$

$$\gamma^{-1} = 9.76 \text{ nm}$$

$$\varphi = 0.1 \text{ meV}$$

$$v_{dens} = 5 \times 10^6 \text{ mm}^{-3}$$

$$v_{rMax} = \text{varies as per legend}$$

$$r_i = 100 \text{ nm}$$

Parameters for Figure 4.14

$$\phi = \text{varies as per legend}$$

$$r = 65 \text{ nm (log normal deviation target = 15\%)}$$

$$G_0 = 4.62 \mu\text{S}$$

$$\gamma^{-1} = 9.76 \text{ nm}$$

$$\varphi = 0.1 \text{ meV}$$

$$v_{dens} = 5 \times 10^6 \text{ mm}^{-3}$$

$$v_{rMax} = 1.0625 \text{ } \mu\text{m}$$

$$r_i = \text{varies as per x-axis}$$